Hydrol. Earth Syst. Sci. Discuss., 11, 13479–13539, 2014
www.hydrol-earth-syst-sci-discuss.net/11/13479/2014/
doi:10.5194/hessd-11-13479-2014

Hydrology and Earth System Sciences
Open Access
Discussions

Evaluation of an extreme-condition-inverse calibration remote sensing model for mapping energy balance fluxes in arid riparian areas

S.-H. Hong[1,*], J. M. H. Hendrickx[1], J. Kleissl[2], R. G. Allen[3], W. G. M. Bastiaanssen[4], R. L. Scott[5], and A. L. Steinwand[6]

[1]New Mexico Tech, Socorro, NM, USA
[2]University of California, San Diego, CA, USA
[3]University of Idaho, Kimberly, ID, USA
[4]Delft University of Technology, Delft, the Netherlands
[5]Southwest Watershed Research Center, USDA-ARS, Tucson, AZ, USA
[6]Inyo County, Water Department, Independence, CA, USA
[*]now at: Murray State University, Murray, KY, USA

Received: 22 August 2014 – Accepted: 17 November 2014 – Published: 10 December 2014

Correspondence to: S.-H. Hong (shong4@murraystate.edu)

Published by Copernicus Publications on behalf of the European Geosciences Union.

HESSD
11, 13479–13539, 2014

Abstract

Accurate information on the distribution of the surface energy balance components in arid riparian areas is needed for sustainable management of water resources as well as for a better understanding of water and heat exchange processes between the land surface and the atmosphere. Since the spatial and temporal distributions of these fluxes over large areas are difficult to determine from ground measurements alone, their prediction from remote sensing data is very attractive as it enables large area coverage and a high repetition rate. In this study the Surface Energy Balance Algorithm for Land (SEBAL) was used to estimate all the energy balance components in the arid riparian areas of the Middle Rio Grande Basin (New Mexico), San Pedro Basin (Arizona), and Owens Valley (California). We compare instantaneous and daily SEBAL fluxes derived from Landsat TM images to surface-based measurements with eddy covariance flux towers. This study presents evidence that SEBAL yields reliable estimates for actual evapotranspiration rates in riparian areas of the southwestern United States. The great strength of the SEBAL method is its internal calibration procedure that eliminates most of the bias in latent heat flux at the expense of increased bias in sensible heat flux.

1 Introduction

The regional distribution of the energy balance components, net surface radiation (R_n), soil heat flux (G), sensible heat flux (H) and latent heat flux (LE) in arid riparian areas is critical knowledge for agricultural, hydrological and climatological investigations. However, R_n, G, H and LE are complex functions of atmospheric conditions, land use, vegetation, soils, and topography which cause these fluxes to vary in space and time. Therefore, it is difficult to estimate them at the regional scale (Parlange et al., 1995). Measurement approaches for LE from the land surface including eddy covariance (Kizer and Elliott, 1991), Bowen ratio (Scott et al., 2004) and weighing lysimeters (Wright, 1982) are too expensive and time consuming for continuous application at sufficient

HESSD
11, 13479–13539, 2014

spatial density at the regional scale. These techniques produce LE measurements over small footprints (m^2 to ha) which are difficult to extrapolate to the regional scale, especially over heterogeneous land surfaces (Moran and Jackson, 1991). For example, in the heterogeneous landscape of the central plateau of Spain as many as 13 ground measurements of evapotranspiration in a relatively small area of 5000 km^2 were not sufficient to predict accurately the area-averaged evapotranspiration rate (Pelgrum and Bastiaanssen, 1996).

Reliable regional estimates of spatial patterns of LE can only be obtained by satellite image-based remote sensing algorithms as has been shown by a number of investigators (e.g. Choudhury, 1989; Granger, 2000; Moran and Jackson, 1991; Kustas and Norman, 1996; Du et al., 2013). Today a variety of LE remote sensing algorithms exists with different spatial (30 m to 1/8° or 13 km in New Mexico) and temporal (daily to monthly) scales: the North American Land Data Assimilation Systems (NLDAS) (Cosgrove et al., 2003), the Land Information Systems (LIS) (Peters Lidard et al., 2004), the Two-Source Energy Balance model (TSEB) (Norman et al., 1995), the Hybrid dual source Trapezoid framework Evapotranspiration Model (HTEM) (Yang and Shang, 2013), the Atmosphere–Land Exchange Inverse (ALEXI) (Anderson et al., 1997), the disaggregated ALEXI model (DisALEXI) (Norman et al., 2003), the Surface Energy Balance System (SEBS) (Su, 2002), the MOD16 ET algorithms (Mu et al., 2011), the Simplified Surface Energy Balance (SSEB) (Senay et al., 2013), the Surface Energy Balance Algorithm for Land (SEBAL) (Bastiaanssen, 1995), Mapping EvapoTranspiration at high spatial Resolution with Internalized Calibration (METRIC) (Allen et al., 2007), as well as algorithms without distinct acronyms (Schüttemeyer et al., 2007; Ma et al., 2004; Jiang and Islam, 2001).

SEBAL has been developed and pioneered by Bastiaanssen and his colleagues in the Netherlands during the 1990s (Bastiaanssen, 1995). METRIC has been developed by Allen and his research team in Idaho using SEBAL as its foundation (Allen et al., 2005). Unlike ALEXI and DisALEXI, SEBAL and METRIC do not require spatial fields of air temperature and atmospheric temperature soundings interpolated across the

HESSD
11, 13479–13539, 2014

region of interest; unlike NLDAS and LIS, SEBAL and METRIC do not require land cover maps. However, applications of SEBAL and METRIC are restricted to clear days over areas of unvarying weather, and require some supervised calibration for each image, preventing application at the continental scale such as done by ALEXI, SSEB, MOD16, NLDAS and LIS.

The accuracy of SEBAL and METRIC for evaporation mapping worldwide is typically about ±15 and ±5 % for, respectively, daily and seasonal evaporation estimates (Bastiaanssen et al., 2005; Allen et al., 2011). Such accuracy is obtained by a calibration method that selects a "cold" and "hot" pixel representing extreme thermal and vegetation conditions within an image. After calculation of the energy balance at the two calibration pixels the sensible heat flux H for each pixel is indexed to its satellite measured surface temperature. The economic efficiency of SEBAL and METRIC is remarkable. For example, in the early 1980's co-author Hendrickx was deployed at Niono in the Office du Niger in Mali to determine water requirements for flood irrigated rice. It took him and a team of four field assistants and several graduate students more than two years to measure the seasonal actual evapotranspiration of rice in four irrigation units covering a total area of about 70 ha using non-weighing lysimeters and discharge measurement structures in irrigation and drainage ditches (Hendrickx et al., 1986). In 2008, the seasonal actual evapotranspiration was obtained for all 86 000 ha of the Office du Niger using SEBAL with Landsat imagery of 2006 at an effort of about two expert months without need for an overseas multi-year deployment (Zwart and Leclert, 2010).

Previous validation studies of SEBAL have mainly been conducted in relatively homogeneous agricultural areas and have focused on comparison of daily ET rates estimated from SEBAL and METRIC with ground measurements using lysimeters (Tasumi, 2003; Trezza, 2002), Bowen ratio and eddy covariance methods (Gibson et al., 2013; Du et al., 2013; Bastiaanssen et al., 2002) and scintillometry (Hemakumara et al., 2003; Kite and Droogers, 2000; Kleissl et al., 2009). The overall goal of this study is to conduct a thorough evaluation of the performance of SEBAL in arid riparian areas

HESSD
11, 13479–13539, 2014

in New Mexico, Arizona and California. Here, vast deserts are transected by narrow river valleys covered by a mosaic of irrigated agricultural fields and riparian vegetation (cottonwood, saltcedar, willow, mesquite, Russian olive and salt grasses) which creates a very heterogeneous landscape with a short patch length scale. If SEBAL performs well under these challenging conditions, it is likely to perform well in most arid and semi-arid regions. Another difference with previous studies is our focus on all components of the energy balance during the instant of satellite overpass as well as on a daily basis. We can accomplish this since we have available a quality controlled data set consisting of R_n, H and LE measurements in the riparian areas of the Middle Rio Grande Basin (New Mexico) and R_n, G, H and LE measurements in the riparian areas of the San Pedro Basin (Arizona) and the Owens River Valley (California).

2 Surface Energy Balance Algorithm for Land (SEBAL)

SEBAL is a remote sensing algorithm that evaluates the fluxes of the energy balance and determines LE as the residual

$$\mathrm{LE} = R_n - G - H \quad (1)$$

where R_n is the net radiation flux density [$\mathrm{W\,m^{-2}}$], G is the soil heat flux density [$\mathrm{W\,m^{-2}}$], H is the sensible heat flux density [$\mathrm{W\,m^{-2}}$], and LE ($= \lambda \mathrm{ET}$) is the latent heat flux density [$\mathrm{W\,m^{-2}}$], which can be converted to the ET rate [$\mathrm{mm\,day^{-1}}$] using the latent heat of vaporization of water λ [$\mathrm{J\,kg^{-1}}$] and the density of water ρ_w [$\mathrm{kg\,m^{-3}}$].

To implement SEBAL, images are needed with information on reflectance in the visible, near-infrared and mid-infrared bands as well as emission in the thermal infrared band. Such images are offered by a number of satellites such as Land Satellite (Landsat), Moderate Resolution Imaging Spectroradiometer (MODIS), Advanced Very High Resolution Radiometer (AVHRR), Advanced Spaceborne Thermal Emission and Reflection Radiometer (ASTER), ENVISAT-Advanced Along Track Scanning Radiometer

HESSD
11, 13479–13539, 2014

(AATSR) and China–Brazil Earth Resources Satellite (CBERS). In this study, we use Landsat images for their high spatial resolution. In undulated landscapes and mountains, a Digital Elevation Model (DEM) is also needed to take into account terrain slope and aspect of each pixel. Extensive descriptions of SEBAL and METRIC have been presented in the literature (Bastiaanssen et al., 1998a; Hong, 2008; Allen et al., 2007). Therefore, we refer to these publications and the PhD dissertation by Hong (2008) for the full details of our SEBAL implementation. Here below we only discuss a critical portion of the SEBAL algorithm.

R_n and G are determined using standard approaches similar to other LE remote sensing algorithms but SEBAL and METRIC have a different unique method for the estimation of the sensible heat flux density H defined as (Brutsaert et al., 1993)

$$H = \frac{\rho_a \cdot c_p \cdot (T_{aero} - T_a)}{r_{ah}} \quad (2)$$

where ρ_a is the density of air [kg m^{-3}], c_p is the specific heat capacity of air [J kg^{-1} K^{-1}], T_{aero} is the aerodynamic surface temperature, T_a is the air temperature measured at a standard screen height, and r_{ah} is the aerodynamic resistance to heat transfer [s m^{-1}]. SEBAL and METRIC overcome the challenge of inferring the aerodynamic surface temperature from the radiometric surface temperature and the need for near-surface air temperature measurements by directly estimating the temperature difference ΔT between T_1 and T_2 taken at two levels z_1 (0.10 m) and z_2 (2 m) above the canopy or soil surface without calculation of the absolute temperature at a given height.

$$H = \frac{\rho_a \cdot c_p \cdot \Delta T}{r_{ah12}} \quad (3)$$

where r_{ah12} is the aerodynamic resistance between levels z_1 and z_2. The ΔT gradient essentially "floats" over the surface. The temperature difference for a dry surface without evaporation (the "hot" pixel) is obtained from the energy balance equation

HESSD
11, 13479–13539, 2014

(Eq. 1) with LE set to zero so that $H = R_n - G$ followed by the inversion of Eq. (3) to $\Delta T = H r_{ah12}/(\rho_a c_p)$. On the other hand, for a wet surface (the "cold" pixel) all available energy $R_n - G$ is assumed in traditional applications of SEBAL to be used for evapotranspiration so that $H = 0$ and $\Delta T = 0$ (Bastiaanssen et al., 1998a; Bastiaanssen, 2000). The implicit assumption in extreme-condition-inverted-calibration processes such as SEBAL and METRIC is that land surfaces with a high ΔT are associated with high radiometric temperatures and those with a low ΔT with low radiometric temperatures. Field measurements in Egypt and Niger (Bastiaanssen et al., 1998b), China (Wang et al., 1998), and USA (Franks and Beven, 1997) have shown that the relationship between T_s and ΔT is approximately positively linear for different field conditions including irrigated fields, deserts and mountains.

$$\Delta T = c_1 \cdot T_s + c_2 \quad (4)$$

where c_1 and c_2 are the linear regression coefficients valid for a landscape at the time and date the image is taken. By using the values of ΔT calculated for the cold and hot pixel the regression coefficients c_1 and c_2 can be determined so that the extremes of H are constrained and outliers of H-fluxes are prevented. The Eq. (4) is dependent upon spatial differences of the radiometric surface temperature rather than absolute surface temperatures to derive maps of the sensible heat flux which minimizes the need for atmospheric corrections as well as uncertainties in surface emissivity, surface roughness and differences in T_{aero} and T_s on H estimates (Allen et al., 2007).

Besides ΔT the other unknown in Eq. (3) is the aerodynamic resistance to heat transfer r_{ah12} which is affected by wind speed, atmospheric stability, and surface roughness. Since r_{ah12} is needed to calculate H while H is required to calculate r_{ah12} , an iterative process is used to find H (Allen et al., 2007; Hong, 2008). Then, after inserting R_n, G and H into Eq. (1) the latent heat flux LE is obtained for each pixel. Finally, dividing LE by the latent heat of vaporization of water yields the instantaneous ET ($mm\,h^{-1}$) at the time of the Landsat overpass around 10:30 a.m.

HESSD
11, 13479–13539, 2014

SEBAL produces an estimate of the instantaneous LE at the time of the satellite overpass. However, for most hydrological applications the daily LE is needed; so the instantaneous LE needs to be extrapolated to the daily LE which is done using the instantaneous evaporative fraction (EF_{inst}). Where soil moisture does not significantly change and advection does not occur, the evaporative fraction has been shown to be approximately constant during the day (Crago, 1996; Farah et al., 2004). However, analysis of field measurements by other investigators (Teixeira et al., 2008; Anderson et al., 1997; Sugita and Brutsaert, 1991) indicates that the instantaneous evaporative fraction on clear days at satellite overpass time (around 10:30 a.m.) tends to be approximately 10–18 % smaller than the daytime average. Therefore, a correction coefficient c_{EF} is introduced to take into account differences between instantaneous and daily evaporative fractions. Some investigators use c_{EF} of 1.00 (Bastiaanssen et al., 2005) while otherssuggest c_{EF} of 1.10 (Anderson et al., 1997) or c_{EF} of 1.18 (Teixeira et al., 2008). The value for c_{EF} should depend on the relative amount of advection of heat, which in turn is a function of regional evaporation, wind speed and relative humidity.

$$EF_{inst} \cdot c_{EF} = \frac{R_n - G - H}{R_n - G} \cdot c_{EF} = \frac{LE_{inst}}{LE_{inst} + H_{inst}} \cdot c_{EF} = EF_{24} \quad (5)$$

Assuming c_{EF} of 1.0 and daily soil heat flux G_{24} [MJ m^{-2} day^{-1}] close to zero, multiplication of the instantaneous EF_{inst} determined from SEBAL with the total daily available energy yields the daily ET rate in mm per day (Bastiaanssen et al., 1998a) as

$$ET_{24} = \frac{EF_{inst} \cdot (R_{n24} - G_{24})}{\lambda \cdot \rho_w} \approx \frac{EF_{24} \cdot R_{n24}}{\lambda \cdot \rho_w} \quad (6)$$

where ET_{24} is daily ET [mm day^{-1}], ρ_w is the density of water [kg m^{-3}] and R_{n24} is daily net radiation [MJ m^{-2} day^{-1}] obtained by an semi-empirical expression (De Bruin, 1987) as described by (Hong, 2008). Finally, the daily H_{24} is not derived from the instantaneous H but is calculated as the difference between R_{n24} and LE_{24}.

HESSD
11, 13479–13539, 2014

3 Method and materials

3.1 Study areas

The components of the energy balance (R_n, G, H and LE) are determined by SEBAL from sixteen Landsat 7 images of year 2000 to 2003 for three typical riparian areas in the southwestern United States located in the Middle Rio Grande Valley (NM), the Owens Valley (CA) and the San Pedro Basin (AZ) (Table 1).

The Middle Rio Grande Valley extends through central New Mexico and is defined as the reach of the Rio Grande between Cochiti Dam and Elephant Butte Reservoir. The Middle Rio Grande riparian vegetation consists of cottonwood and salt grasses as well as various non-native species including saltcedar and russian olive. In the Middle Rio Grande Valley, the average annual air temperature is 15 °C. Daily summer temperatures range from 20 to 40 °C, while daily winter temperatures range from −12 to 10 °C. Mean annual precipitation is about 25 cm and mean annual potential evapotranspiration is approximately 170 cm.

The Owens Valley is a long, narrow valley on the eastern slope of the Sierra Nevada in Inyo County, California. It is a closed basin drained by the Owens River which terminates at saline Owens Lake. The Owens Valley has a mild high-desert climate: in summer (June, July and August) the lowest average daily minimum temperature is 7 °C and the highest average daily maximum temperature temperatures is 37 °C, and in winter (November to February) from −7 to 21 °C. Since, the Owens Valley is located in the "rain shadow" of the Sierra Nevada, the average annual precipitation in the Owens Valley is only about 12 cm and mean annual potential evapotranspiration is about 150 cm. Snowmelt runoff from the Sierra Nevada creates a shallow water table underneath the valley floor which supports approximately 28 000 ha of native shrubs and grasses in riparian areas.

The San Pedro Basin begins in Sonora, Mexico and extends to where the river flows into the Gila in southern Arizona. The river is surrounded by vegetation consisting of Cottonwood, Willow, Mesquite and Sacaton grass. The mean air temperature of the

HESSD
11, 13479–13539, 2014

Upper San Pedro valley is around 18 °C. Daily summer temperatures range from 22 to 44 °C, while daily winter temperatures range from 9 to 24 °C. Mean annual precipitation is about 35 cm and mean annual potential evapotranspiration is approximately 170 cm.

Although, the regional climate of all three areas is classified as arid/semiarid, there exists a difference in precipitation pattern. In the Owens Valley, precipitation occurs primarily in winter and spring, while in the San Pedro and the Middle Rio Grande Valleys, the annual precipitation distribution is bimodal, with more than half of the rainfall being monsoonal in summer, although the proportion varies considerably from year to year (Cleverly et al., 2002; Elmore et al., 2002; Scott et al., 2000; Stromberg, 1998; Costigan et al., 2000). Table 2 presents main characteristics of the study sites: vegetation type, elevation above sea level, height of vegetation canopy and the height of flux sensors above ground level. The average elevations are 1440, 1230 and 1220 m above sea level for, respectively, the Middle Rio Grande Basin, Owens Valley and San Pedro Valley.

3.2 Eddy covariance measurements and closure forcing

SEBAL estimates of LE, H, G, and R_n are compared to ground-based eddy covariance and energy balance measurements. At each site, the turbulent heat fluxes were measured using the eddy covariance (EC) method that theoretically provides direct and reliable measurements of H and LE (Arya, 2001). At all sites, a three-dimensional sonic anemometer-thermometer that measures the three-dimensional wind vector and virtual temperature, was collocated with a Krypton hygrometer or open path infrared gas analyzer that measures water vapor density [g m^{-3}] with a sampling rate of 10 Hz (Cleverly et al., 2002; Steinwand et al., 2006; Scott et al., 2004). The covariances between the vertical wind speed and, respectively, water vapor density and virtual air temperature are used for the computation of, respectively, 30 min averages of the latent heat flux LE and the sensible heat flux H. The installed eddy covariance systems are oriented toward the predominant wind direction, thereby reducing data loss due to winds blocked by the tower and instrumentation. All eddy covariance data were quality

HESSD
11, 13479–13539, 2014

controlled and corrected for tilt by coordinate rotations, frequency response, oxygen absorption of the Krypton hygrometer, and flux effects on air density. The coordinate rotation, however, cannot correct for effects of changing wind direction during 30 min average periods that can cause mean "vertical" wind speeds to deviate from 0, thereby inducing error in the H and LE measurements. This problem is common to EC measurements in tall vegetation such as trees where the sensors are placed too close to tree branches or canopy. Soil heat fluxes in the San Pedro Valley and Owens Valley were obtained from measurements using soil heat flux plates that were corrected for soil heat storage above the plate using collocated soil temperature and soil moisture measurements.

At the Middle Rio Grande sites, soil heat storage could not be calculated due to the absence of soil moisture measurements. Therefore, the soil heat flux measurements in the Middle Rio Grande Valley have not been compared with those estimated by SEBAL. The net radiation was obtained from REBS Q7 or Kipp and Zonen CNR1 net radiometers. In some of the installations, the R_n sensors may have been mounted too close to the towers and may have been impacted by reflection from the local structure. For the comparison of the 30 min averaged ground measurements with the instantaneous energy fluxes estimated using SEBAL, an "instantaneous" ground measurement was determined by linear interpolation between the two 30 min averaged, ground measurements before and after the satellite overpass. To compute daily values of LE, H, G and R_n the 30 min flux data were summed over the day (00:00–24:00 LT).

We use the relative closure of the energy balance (Twine et al., 2000) as a criterion for the selection of high-quality R_n, G, H, and LE ground measurements for comparison with SEBAL estimates. Figure 1 presents the relative closures calculated for satellite overpass days for all sites as provided by the investigators operating the EC towers in the Owens and San Pedro River Valleys. Since no soil heat flux measurements were available in the Middle Rio Grande Valley, we calculated the instantaneous relative closure [%] using the instantaneous soil heat flux derived by SEBAL instead of the ground measured soil heat flux. This approach is justified on the basis of the rea-

HESSD
11, 13479–13539, 2014

sonable agreement found between SEBAL derived instantaneous soil heat fluxes and those measured on the ground in the Owens and San Pedro River Valleys (Table 5). If the sum of H and LE, before correction, was less than 65 % or greater than 110 % of the available energy ($R_n - G$), the data were not used in our analysis. This criterion leads to the exclusion of 45 % of instantaneous fluxes and 39 % of the daily fluxes of the data from the Middle Rio Grande Valley, 79 % (instantaneous) and 43 % (daily) from the Owens River Valley and 17 % (instantaneous) and zero % (daily) from the San Pedro River Valley. The remaining turbulent heat flux estimates are improved thru forcing the closure of the energy balance by increasing LE and H by the Bowen ratio (Twine et al., 2000). The improved adjusted H and LE are identified as H_{adj} and LE_{adj}.

After elimination of EC measurements on the basis of unacceptable closures, we eliminated also the EC measurements taken on 16 May 2003 in the San Pedro River Valley at the Mesquite (CM) site. On this day the wind direction was approximately 90° different from the prevailing wind direction which resulted in fetch distances considerably shorter than the recommended 100 times the sensor height above the canopy (Stannard, 1993; Sumner and Jacobs, 2005). The problem was exacerbated by the relatively high placement (7 m) of the sensors above the canopy (Table 2) since the heat fluxes can vary significantly with height under such conditions (De Bruin et al., 1991).

3.3 Comparison of SEBAL flux predictions to ground measurements

Comparison of SEBAL derived estimates of R_n, G, H and LE with ground measurements is not a straightforward operation because the spatial and temporal scales of the SEBAL predictions and ground measurements are quite different. In this section we will discuss these scale gaps for each flux in the energy balance.

3.3.1 Net radiation

R_n is measured with a net radiometer at a height of about 2–3 m above the canopy (Table 2) that covers typically an observation area on the order of 10 m^2. The measure-

HESSD
11, 13479–13539, 2014

ments are taken every second and made available as 30 min averages for this study. The SEBAL R_n prediction is derived from reflectances in the visible, near-infrared and mid-infrared bands from a 900 m^2 pixel as well as the emittance in the thermal band from a 3600 m^2 pixel. Thus, the R_n ground observation is based on a measurement area at least two orders of magnitude smaller than the SEBAL prediction. For homogeneous areas this difference will not matter much but for heterogeneous areas it may cause serious bias, since the satellite based R_n samples a larger area and is therefore more representative of the EC footprint. In riparian areas heterogeneity is the rule rather than exception. Radiometers are typically placed over the canopy of interest which may cause under-representation of surrounding bare soil or ground cover in the angle of view. Therefore, ground measured R_n is expected to be biased towards the R_n of the vegetation of interest.

3.3.2 Soil heat flux

G is measured by soil heat flux plates combined with the determination of changes in heat storage above the plate using soil temperature and soil water content measurements. If G is not corrected for heat storage above the plate, large errors will result (Sauer, 2002a). This is the case for the measurements at the Middle Rio Grande sites and, therefore, these G measurements have not been used for the comparison. The measurement area of a soil heat flux plate is about 0.001 m^2 which is almost six orders of magnitude less than a 900 m^2 Landsat pixel. G is spatially variable due to heterogeneity in soil moisture and vegetation cover, so that numerous flux measurements would be needed to estimate the average pixel G with the desired accuracy (Kustas et al., 2000; Humes et al., 1994). Therefore, we expect the instantaneous G ground measurements to be a rather crude estimation of the true instantaneous G of a pixel. The instantaneous G can vary widely depending on soil condition (20–300 $W\,m^{-2}$) (Sauer et al., 2003). Since G is positive during the day and negative during the night the daily G is rather small compared to the other components of the energy

HESSD
11, 13479–13539, 2014

balance (Seguin and Itier, 1983). G is measured in the field every second; we used averages of 30 min for this study.

3.3.3 Sensible and latent heat fluxes

H and LE are measured using a three-dimensional sonic anemometer-thermometer and Krypton hygrometer, respectively (or open patch infrared gas analyzer). For these components of the energy balance the relationship between ground measurement area and pixel size is the opposite of the one discussed for R_n and G: the area of ground measurements is several times larger than a Landsat pixel. As discussed in Sect. 3.4 a typical footprint for H and LE under the micrometeorological conditions of this clear-sky study covers about 5 pixels or about 4500 m^2. The location of the footprint is upwind of the EC tower and its size and distance from the tower depends on atmospheric stability. For the comparison of H and LE SEBAL estimates with ground measurements, first the footprint area must be determined and then, the weighted average is taken of the SEBAL estimated H and LE values of all pixels within the footprint area. These weighted averages of H and LE are compared with the ground measured H and LE at the EC tower. This approach is expected to work reasonably well for comparison of SEBAL instantaneous H and LE estimates with ground measurements at the time of the satellite overpass.

Comparison of daily H and LE fluxes is problematic. Instantaneous H and LE measurements are available at the EC tower as 30 min averages but SEBAL estimates of the instantaneous H and LE are only available once per image day at the time of the satellite overpass. Therefore, it is impossible to compare every 30 min the footprint averaged SEBAL estimates with the ground measurements. It is also problematic to compare daily SEBAL estimates of H and LE at each pixel with daily H and LE measurements at the EC tower. Daily H and LE measurements at the EC tower are the daily sum of 30 min instantaneous H and LE measurements originating from different footprints covering a wide area especially on days with highly variable wind directions. Combining the assumption of constant evaporative fraction during the day with the daily

HESSD
11, 13479–13539, 2014

footprint using daily-averaged parameters including air temperature, u^*, wind speed and direction, it may be possible to compare daily H and LE measurements at the tower with SEBAL estimates. However, uncertainties would remain and at best a rough comparison can be made since the average daily values are not necessarily a good measure for determination of a daily footprint. Therefore, in this study rather than trying to determine the true location of the "representative" daily foot print, the daily H and LE ground measurements will be compared with the average SEBAL estimated H and LE fluxes originating from twenty-five homogeneous pixels surrounding the EC tower. The homogeneity of the pixels surrounding the tower was evaluated by inspecting NDVI, albedo, and surface temperature values as well as the H and LE values themselves.

3.3.4 Quantitative measures to compare SEBAL estimates and ground measurements

The numerical comparison of the energy balance components (R_n, G, H, and LE) estimated by SEBAL with those measured on the ground is conducted by means of quantitative measures proposed by Willmott and others for the validation of atmospheric models (Willmott, 1981, 1982; Fox, 1981). We use the coefficient of determination (r^2), mean absolute difference (MAD), root mean square difference (RMSD), and the mean relative difference (MRD) (Hong, 2008). The coefficients of determination may be misleading as "high" or statistically significant values of r are often unrelated to the sizes of the differences between model estimates and measurements (Willmott and Wicks, 1980). In addition, the distributions of the estimates and measurements will often not conform to the assumptions that are prerequisite to the application of inferential statistics (Willmott, 1982). However, since r^2 is a commonly used correlation measure that reflects the proportion of the "variance explained" by the model, we report this measure. The MAD and RMSD are robust measures as they summarize the mean differences between SEBAL estimates and ground measurements; the MAD is less sensitive to outliers than RMSD. The MRD is often used as an indication how well SEBAL estimates agree with ground measurements (Bastiaanssen et al., 2005).

HESSD
11, 13479–13539, 2014

3.4 Footprint model

The location and extent of the footprint depends on surface roughness, atmospheric stability, wind speed, wind direction and may cover many pixels upwind of the eddy covariance tower (Schmid and Oke, 1990; Hsieh et al., 2000). There are several types of footprint models. Initially, simple two-dimensional analytical footprint models for neutral atmospheric conditions were developed (Gash, 1986; Schuepp et al., 1990). Later, the analytical footprint model was improved to account for atmospheric stability conditions (Horst and Weil, 1992; Hsieh et al., 2000). The footprint flux, $F_{(x,z_s)}$ [–], along the upwind direction, x [m], measured at the height z_s [m], suggested by (Hsieh et al., 2000) is used in this study.

A typical footprint size and footprint intensity for one 30 min period on 19 August 2002, at a Rio Grande saltcedar EC tower is presented in Fig. 2. To verify the quality of the footprint model used in this study, we also calculated x_{max} (peak footprint) for this period with the model by Schuepp et al. (1990). The models by Hsieh et al. (2000) and Schuepp et al. (2000) calculate x_{max} as 10 m (Fig. 2) and 11 m, respectively, which implies that the footprint from Hsieh et al. (2000) is indeed close to the tower. At most EC sites, the maximum contribution to the footprint was within 50 m from the tower (wind speeds were generally less than 4 ms^{-1}) and most of the footprint intensity (> 90 %) is located within 300 m from the tower. We compute the footprints from meteorological parameters including air temperature, sensible heat flux, wind speed, wind direction and friction velocity. The footprints for H and LE are obtained for the time of the satellite overpass using the 30 min averaged meteorological parameters. Approximately 80 % of all footprint fluxes cover an area of 5 to 9 pixels, twenty percent cover larger areas. As explained in Sect. 3.3.3 calculation of a representative daily footprint for comparison of SEBAL H and LE estimates and ground measurements is nearly impossible. Therefore, the use the average H and LE values of the 25 pixels surrounding the EC tower pixel is considered to be the best option for the comparison of daily ground measurements and SEBAL estimates.

HESSD
11, 13479–13539, 2014

3.5 Calibration and evaluation of SEBAL flux predictions

This study cannot be a robust validation study due to missing soil heat flux measurements in the Middle Rio Grande Valley and biased net radiation measurements over heterogeneous riparian vegetation with patches of bare soil. Our aim is to evaluate the challenges of SEBAL flux predictions in arid riparian areas using a validation approach.

Calibration is the process of adjusting hydrologic model parameters to obtain a fit to observed data. In SEBAL the relationship between model parameter ΔT and remotely observed radiometric surface temperature T_s in Eq. (4) is calibrated using the remotely observed energy balance components of R_n and G at two extreme conditions in a Landsat image: the cold wet pixel and hot dry pixel.

After calibration, validation tests typically are applied to a second set of data to test the performance of a hydrologic model. In the context of this study the second data set consists of ground measurements of R_n, G, H and LE, at pixels other than the cold and hot pixels. Validation or evaluation is accomplished by comparing the SEBAL predicted energy balance components with the ones measured on the ground at locations with eddy covariance towers.

Calibration approaches

The temperatures of the cold and hot pixel for the derivation of calibration coefficients c_1 and c_2 in Eq. (4) are most critical in SEBAL as well as METRIC since they constrain LE between its maximum value at the cold wet pixel and zero at the hot dry pixel by reducing biases in H associated with uncertainties in aerodynamic characteristics including T_s (Bastiaanssen et al., 2005; Allen et al., 2006). In SEBAL this calibration is entirely based on information that is available inside the image and, therefore, it is called "self-calibration" (Bastiaanssen et al., 2005) or "internalized calibration" and "autocalibration".

Over the cold pixel it is assumed that $\Delta T = 0$, which implies that $H = 0$ and LE = $R_n - G$. An alternative manner in METRIC is to use high quality hourly meteorological

HESSD
11, 13479–13539, 2014

observations for the calculation of the reference ET (Allen et al., 1998) for the estimation of H in well-irrigated alfalfa and clipped grass fields (Allen et al., 2007, 2011). However, this study deals with a SEBAL application in riparian areas without high quality hourly meteorological observations as is the default condition for many regions worldwide (Droogers and Allen, 2002). The selection of the hot pixel is quite challenging because the heterogeneous landscapes of the southwestern US include quite a few hot and dry areas with a wide range of temperatures. In this study, the hot pixel is selected from a dry bare agricultural field where ET is just close to zero. Therefore, for any pixel cooler than the hot pixel, ET > 0 (if the R_n and G are the same), and for any pixel warmer than the hot pixel, for example a parking lots, ET = 0. In addition, the equation for G estimation was derived for agricultural conditions and therefore produces more dependable estimates for calibration when applied to a bare, agricultural soil having a tillage history.

As a consequence of the "internalized calibration" any biases in R_n or G at the hot pixel in the image are transferred into H. However, this bias introduced into H is transferred back out of the energy balance during the calculation of LE from Eq. (1), since the bias is present in both $R_n - G$ and H, and thus cancels (Allen et al., 2006). The "internalized calibration" results in the least biased LE if the cold and hot pixel are properly selected and is the most distinctive feature of SEBAL and METRIC compared to other remote sensing LE algorithms.

The selection of cold and hot pixel requires a thorough understanding of field micrometeorology and is somewhat subjective, i.e. different experts will select slightly different temperature values. The cold pixel is selected where areas with well-watered healthy crops with full soil cover or in shallow water bodies (Allen et al., 2011; Bastiaanssen et al., 2005) and is relatively straightforward while the hot pixel selection is more challenging. Therefore, it has been proposed to use micrometeorological ground measurements of energy balance components for the calibration and validation of remote sensing algorithms such as SEBAL (Kleissl et al., 2009). However, due to the relatively large uncertainties of ground measured sensible and latent heat fluxes (Loescher

HESSD
11, 13479–13539, 2014

et al., 2005; Kleissl et al., 2008) the value of ground measurements for calibration of SEBAL is not well established. For this reason we test two different calibration approaches for the selection of the temperatures for the cold and hot pixel: the *Empirical* (EM) *approach* and the *Eddy Covariance* (EC) *approach*. The former is based on inspection of the hydrogeological features of the landscape and qualitative micrometeorological considerations and is typical for most SEBAL applications since the high number of EC towers available in this study is a unique situation. The Eddy Covariance (EC) approach is based on inspection of the hydrogeological features of the landscape followed by fine-tuning the parameters c_1 (slope) and c_2 (intercept) in Eq. (4) using ground measurements of instantaneous latent heat fluxes at the EC towers after adjustment for closure error. Since selection of the cold pixel is straightforward in fully vegetated fields, the temperature of the cold pixel was fixed but the temperature of the hot pixel was varied to best match the instantaneous ground measurements of LE (Hong, 2008). In order to independently evaluate the EM vs. the EC approach, senior author Hong implemented the EC approach, while co-author Hendrickx implemented the EM approach.

Five different calibration scenarios (S1–S5) were implemented and compared (Table 3). In the EC approach, calibration of SEBAL to ground measurements was implemented either using the average footprint weighted instantaneous SEBAL LE heat fluxes (S1, EC_FP) or using the instantaneous SEBAL LE heat flux of the pixel where the EC tower is located (S2, EC_TP). The former method is difficult to implement for most practitioners while the latter is practical and fast but requires homogeneous conditions around the tower to the maximum extent of the footprint. The EM approach (S3) was implemented without using the LE's measured by the EC towers or any other meteorological measurements.

In Sect. 3.3.1 it was hypothesized that the ground measured R_n may be biased towards vegetation while the SEBAL R_n may be more representative for the true R_n of a pixel covered with vegetation and bare soil patches. In Sect. 4 strong evidence is presented that the SEBAL R_n (SR_n) is more accurate. Therefore, we also evaluated the

HESSD
11, 13479–13539, 2014

impact of using the more accurate SR_n for energy balance closure in the EC approach on the tower pixel (S4, EC_TP/SR_n) and in the EM approach (S5, SR_n).

4 Results and discussion

4.1 Spatio-temporal distribution of daily latent heat fluxes

Figure 3 presents an example of the ET maps produced by SEBAL. Similar maps for the other components of the energy balance as well as other environmental parameters such as albedo, NDVI, surface temperature, etc. can be generated. In Fig. 3, daily ET rates are mapped in the Middle Rio Grande Valley and surrounding deserts on four different days during the spring, summer and fall. The maps show how the ET rates increase from 7 April (just after the start of the irrigation season) to 16 June at the height of the irrigation season; a decrease of ET is observed during September and October when fields are harvested and lower temperatures are impeding crop growth. On all four days higher ET rates are observed over irrigated fields and in the riparian areas while low to very low rates occur in the surrounding deserts.

4.2 Comparison of SEBAL net radiation with ground measurements

Figures 4 and 5 and Table 4 present the comparisons of the instantaneous and daily R_n measured on the ground and estimated by SEBAL. The MADs are 88/87 and 97 W m^{-2} for the EC approaches (S1/S2) and Empirical Approach (S3), respectively, resulting in MRDs of 13.0/12.8 and 14.6 %. These differences are about two to three times larger than those typically reported for SEBAL (Jacob et al., 2002; Allen et al., 2006). The much larger than usual MRD is attributed to the heterogeneity of the riparian sites, the different footprints of net radiometer and Landsat pixel, and the preferential positioning of the net radiometer over vegetation (Sect. 3.3.1). The higher net radiation measured on the ground as compared with the SEBAL net radiation supports this argument.

HESSD
11, 13479–13539, 2014

A bias occurs where the net radiometer is placed preferentially above vegetation that has a lower albedo, lower surface temperature and higher surface emissivity than the patches of bare soil next to the vegetation in the Landsat pixel. Increasing MRDs with increasing heterogeneity of the land surface have been observed in Arizona where the MRD's between ground measured R_n's and the one's estimated with a remote sensing algorithm were 1.2, 9.2, and 17.2 %, respectively, for a homogeneous cotton field, heterogeneous shrub terrain, and heterogeneous grassland (Su, 2002). The MRD of 9.2 and 17.2 % from the heterogeneous pixels are similar to the ones reported in Table 4.

Contrary to the instantaneous values, the daily net radiations measured on the ground and determined in SEBAL match very well with MRDs of only −2.3 to −2.9 %. This immediately begs the question "why?" since the instantaneous R_n's differ by more than 12 %. On clear days over sparsely vegetated surfaces the maximum temperature difference between bare soil and vegetation typically occurs around noon. For example, temperature differences measured in the Walnut Gulch Experimental Watershed near Tombstone, Arizona, varied between 10 and 25 °C during that time of the day (Humes et al., 1994). Since the conditions in the arid riparian areas of this study are similar, we expect similar temperature differences to occur when the satellite passes over around 10:30 a.m. The incoming short and longwave radiation are equal for the bare soil and the vegetation; therefore the net radiation will depend on the outgoing short and long wave radiation. The albedo and surface temperature of dry bare soils during the day are higher than of vegetation resulting in more reflection of short wave radiation and more emission of long wave radiation which results in a lower R_n during the day for bare soil. During the night the surface temperatures of vegetation and bare soil are similar so that –due to the higher emissivity of vegetation (0.99) as compared to bare soil (0.94) (Humes et al., 1994) – the R_n of vegetation is lower. Using the equations presented by (Hong, 2008) one can roughly calculate that the daily R_n difference between vegetation and soil will be considerably smaller than the instantaneous R_n difference around 10:30 a.m.

HESSD
11, 13479–13539, 2014

These differences have been quantified by comparing the SEBAL estimated instantaneous and daily net radiation for fully vegetated agricultural fields, saltcedar, and bare soils (Table 5). Whereas the measured instantaneous net radiation fluxes of fully cropped agricultural fields and saltcedar stands exceeded those of bare soils by 54 to 77 %, the daily net radiation fluxes were only 20 to 36 % larger. A typical Leaf Area Index (LAI) for saltcedar in the Middle Rio Grande Valley is about 2.5 (Cleverly et al., 2002) which indicates that bare soil is present but vegetation cover is dominant. Now let us assume a typical mixed pixel with a soil cover of 75 % saltcedar and 25 % bare soil. The data from Table 5 for the first saltcedar plot show that the ratios between 100 % saltcedar and 100 % bare soil for, respectively, instantaneous and daily net radiation are 1.77 and 1.34. We want to find similar ratios between 100 % saltcedar and our mixed pixel using the values of Table 5 for the instantaneous and daily net radiation for saltcedar and bare soil. Ignoring the effect of thermal radiation from soil that is intercepted by adjacent vegetation, the instantaneous and daily net radiations for the mixed pixel are, respectively, $0.75 \times 670 + 0.25 \times 379 = 598\,\mathrm{W\,m^{-2}}$ and $0.75 \times 19.8 + 0.25 \times 14.8 = 14.9 + 3.7 = 18.6\,\mathrm{MJ\,m^{-2}\,day^{-1}}$. So, the net instantaneous and daily radiations of a fully vegetated saltcedar pixel are 670/598 = 1.12 and 19.8/18.6 = 1.06 times those of our mixed pixel. The 12 % difference is similar to the MRD's of 13–15 % presented for the difference in instantaneous net radiation between ground measurements and SEBAL estimates. The 6 % difference for daily net radiation falls within error ranges of radiation measurements (Halldin and Lundroth, 1992; Field et al., 1992). Thus, the much smaller MRD for daily R_n (−2.3 to 2.9 %) compared to the MRD of instantaneous R_n (about 13 %) can be explained by environmental radiation physics and is not caused by bias in the SEBAL method for determination of instantaneous R_n or in the radiation sensors. This leads to the conclusion that the SEBAL estimated net radiation for the 900 $\mathrm{m^2}$ of the EC tower pixel is more representative for each site than the ground measurements with the net radiation meter preferentially positioned over a 10 $\mathrm{m^2}$ patch of vegetation.

HESSD
11, 13479–13539, 2014

4.3 Comparison of SEBAL soil heat flux with ground measurements

The magnitude of soil heat flux G depends on surface cover, soil water content, and solar irradiance. For a moist soil beneath a plant canopy or residue layer the instantaneous G will often be less than $\pm 20\,W\,m^{-2}$ (Sauer, 2002b) while a bare, dry, exposed soil in midsummer could have a day-peak in excess of $300\,W\,m^{-2}$ (Fuchs and Hadas, 1973). In the Middle Rio Grande Basin during summer typical midday (10 a.m. through 2 p.m.) values of G are 104 and $132\,W\,m^{-2}$ for, respectively, upland grassland and shrubs (Kurc and Small, 2004). These values demonstrate that the instantaneous G in riparian areas can be an important component of the instantaneous energy balance that needs to be taken into account. In most field soils the instantaneous G exhibits not only a temporal variability but also a large spatial variability which makes it very difficult to measure an average G for areas with the size of a typical Landsat pixel ($30\,m \times 30\,m$) (Sauer, 2002b).

For this study six soil heat flux measurements were available from the Owens Valley and the San Pedro Valley. The SEBAL determined G approaches the ground measured G reasonably well (Fig. 6) but the MRD is relatively high with values of 30.9 to 32.2 % (Table 6). However, the overall impact of the relatively high MRD in instantaneous G is minor since its MAD of $35\,W\,m^{-2}$ (Table 6) hovers around 6 % percent of the SEBAL predicted instantaneous net radiation and around 5 % percent of the ground measured instantaneous net radiation. The daily G is close to zero since heat enters the soil during the day but leaves the soil during the night. The daily G measurements in the field confirm this (Table 6). Therefore, it is assumed in SEBAL that the daily heat flux can be neglected, i.e. G is zero.

Given the high spatial and temporal variability of G (Sauer, 2002b) within one Landsat pixel, the reasonable agreement between SEBAL predicted instantaneous G and ground measurements (Fig. 6 and Table 6), the relatively minor impact of an error in G on the estimates of ET, and the impossibility to measure a truly representative G for a $900\,m^2$ heterogeneous riparian pixel using soil heat flux plates with a foot print of only

HESSD
11, 13479–13539, 2014

0.001 m^2, it appears that the SEBAL estimated G results in a quite acceptable estimate on the pixel scale.

4.4 Comparison of SEBAL sensible and latent heat fluxes with ground measurements

Since there is a strong interplay between sensible and latent heat fluxes we discuss both heat fluxes together in this section. First we inspect the plots of instantaneous and daily SEBAL heat flux estimates vs. ground measurements (Fig. 7) that demonstrate several interesting features. Our data set covers a wide range of conditions varying from dry to moist which allows evaluation of SEBAL over a wide range of environmental conditions in riparian areas. The ground measured instantaneous and daily sensible heat fluxes have, respectively, two and six negative data points which is an indication of the occurrence of regional advection. This advection is relatively minor for the instantaneous fluxes during satellite overpass around 10:30 a.m. but increases considerably during late morning and early afternoon as reflected in the daily fluxes. The SEBAL estimated instantaneous and daily sensible heat fluxes that correspond to negative values of the ground measurements are close to zero since the surface temperatures of their pixels are close to the cold pixel's temperature. When high quality hourly meteorological data are available regional advection can be accounted for in SEBAL by defining an advection enhancement parameter that is a function of soil moisture and weather conditions (Bastiaanssen et al., 2006; Allen et al., 2011) or one could implement METRIC (Allen et al., 2007). However, in this study our aim is to evaluate the performance of the traditional SEBAL in heterogeneous arid environments where no weather data are available. The data in Fig. 7 show that ignoring regional advection results in a maximum underestimation of the instantaneous and daily latent heat fluxes by, respectively, about 10 and 20 % under moist conditions; it becomes considerably less when the soil dries out. In this study we have removed all data related to negative instantaneous and daily sensible heat fluxes so that advection effects will not interfere

HESSD
11, 13479–13539, 2014

with our evaluation of the traditional SEBAL approach that does not take advection into account (Allen et al., 2011; Bastiaanssen et al., 1998a).

4.4.1 Comparison of instantaneous heat fluxes

Figures 8 and 9 present plots of, respectively, the adjusted sensible and latent heat fluxes measured at the EC towers vs. the SEBAL estimates resulting from scenarios S1 through S5. While there exists a severe mismatch between the SEBAL estimated instantaneous sensible heat fluxes and the ground measurements (S1–S3), once the SEBAL estimated net radiation is used in the "ground measured" energy balance good agreement is reached (S4 and S5). SEBAL estimated instantaneous latent heat fluxes and ground measurements show good agreement for all five scenarios (S1–S5) including the ones with a poor sensible heat flux match (S1–S3). Table 7 presents the quantitative comparison measures for these instantaneous fluxes. The prediction of latent heat fluxes is good for scenarios S1–S5 with a mean MRD of −5.1 % which is less than the average 14 % instantaneous deviation reported for SEBAL applications worldwide (Bastiaanssen et al., 2005).

The ground measured instantaneous H and LE are identical in S1–S3 but differ slightly from each other in S4 and S5 due to a slight difference in the temperature of the cold pixel that is also used for the estimation of the air temperature for calculation of the incoming long wave radiation. As a result the instantaneous net radiations of S4 and S5 are also slightly different. However, a large difference exists between the ground measured H and LE in S1–S3 vs. those in S4–S5. This is caused by the bias in instantaneous net radiation of the ground measurements vs. the net radiation determined with SEBAL (Table 4). In Table 7 the H and LE SEBAL estimates for the EM approaches (S3 and S5) are identical since this approach does not use the EC measured instantaneous LE for calibration; one set of cold and hot pixels are used for both scenarios in SEBAL. However, in S1, S2 and S4 a different set of cold and hot pixels are determined for each scenario by forcing the constants c_1 and c_2 in Eq. (4) to fit the

HESSD
11, 13479–13539, 2014

instantaneous LE measurements at the EC towers. This leads to quite different *H* and LE SEBAL estimates in S1, S2 and S4.

In scenarios S1 and S2 of Table 7 there is no significant difference between the SEBAL estimated sensible (156 vs. 138 $W m^{-2}$) and latent (314 vs. 333 $W m^{-2}$) heat fluxes. Thus, SEBAL calibrations based on the instantaneous latent heat flux of the tower pixels (S2) or on the latent heat flux of the instantaneous foot prints during the satellite's overpass (S1) yield similar results in this study except that the MAD and RMSD of S1 are lower: MAD/RMSD values for S1 and S2 are 39/57 and 56/74, respectively. This finding is relevant for practitioners who need to calibrate SEBAL on a routine basis and/or in nearly real-time: using only the tower pixels is much faster and easier to implement automatically than determination of a footprint weighted average. It also justifies the omission of foot print scenario S1 from further consideration in scenario S4. However, for posterior SEBAL analyses and research applications use of the footprint is still recommended since (1) it results in somewhat smaller comparison measures (Table 7) and (2) footprint analyses are effective for the detection of unusual environmental conditions.

The MAD and RMSD of the sensible heat fluxes for S1, S2 and S3 are quite similar but rather high with MAD/RMSD values of, respectively, 108/131, 126/147 and 111/135. The values of S4 and S5 36/46 and 61/77 are considerably lower and reflect the ground energy balance correction by using the SEBAL net radiation. The MAD/RMSD values of the latent heat fluxes are increasing from a low value of 39/57 for S1, 56/74 for S2 to 66/81 for S3 while the values for S4 and S5 are, respectively, 39/48 and 61/77. Thus, using the net radiation correction has a much smaller effect for the latent heat fluxes than for the sensible heat fluxes which is a result of the internal calibration of SEBAL. The comparison measures for S3 and S5 (the empirical traditional SEBAL approach) are also very similar for the latent heat flux but are reduced in half for the sensible heat flux after net radiation correction.

Through the "anchoring" of *H* and LE at the cold and hot pixels SEBAL reduces or cancels biases introduced in the calculation of albedo, net radiation, and surface tem-

HESSD
11, 13479–13539, 2014

perature as well as errors in narrow band emissivity, atmospheric correction, satellite sensor, aerodynamic resistance, and soil heat flux function. This can result in a reduction of total bias in ET of as much as 30 % compared to other models that are not routinely internally calibrated (Allen et al., 2006). Allen et al. (2007) describe how METRIC, through the use of weather based reference ET, is able to eliminate most internal energy balance component biases at both the cold and hot extreme conditions. SEBAL, on the other hand, eliminates biases at the hot extreme, but necessarily retains a bias at the cold extreme where it is assumed that LE = $R_n - G$. The cost for the improved estimates for LE is a deterioration of the SEBAL and METRIC H estimates since the sensible heat flux, as an intermediate parameter, absorbs most of the aforementioned biases as a result of the internal calibration process (Choi et al., 2009).

The same trends observed in the MAD and RMSD values are found in the MRD values presented in Table 7. A striking feature in S1–S3 is the very poor prediction of the sensible heat flux with MRD's between 35 and 47 %. Especially, for S1 and S2 that have been calibrated against ground measured instantaneous latent heat fluxes, this result was not expected. The discrepancy is not caused by any error in the SEBAL procedure but by the apparent bias in the ground measurements of the net radiation that was reported earlier (see Sect. 4.2). When the ground measured net radiation is replaced with the arguably more accurate SEBAL estimate of net radiation, the SEBAL estimates of sensible heat fluxes improve dramatically with MRD's in S4 and S5 of, respectively, 0.8 and 16.6 %. Despite the poor MRD's of H (35 to 47 %) in S1–S3 the SEBAL LE estimates exhibit good MRD's (2.7 to −11.5 %). Therefore, these numbers provide an instructive demonstration of the power of SEBAL's internal calibration.

We conclude that calibrating SEBAL with reliable ground measurements at the pixel scale will indeed improve its estimates of both, sensible and latent instantaneous heat fluxes. However, ground measurements of sensible heat fluxes should be used cautiously and carefully for the calibration and evaluation of SEBAL, since the SEBAL sensible heat flux is biased necessarily to compensate for bias in R_n, G and aero-

HESSD
11, 13479–13539, 2014

dynamics, and can deviate from the ground measured sensible heat flux (even if the ground based H is correct) in order to arrive at unbiased estimates of LE.

4.4.2 Comparison of daily sensible and latent heat fluxes

In Fig. 10, the ground measured daily evaporative fraction (EF_{24}) is plotted against the instantaneous evaporative fraction (EF_{inst}). It is clear that the two evaporative fractions are not identical: the daily evaporative fraction is larger than the instantaneous one. Due to the large variability in the data as well as the fact that both the instantaneous and daily evaporative fractions are random variables a straightforward linear regression forced through the origin is not recommended. A simple linear regression with a 5 % significance level yields a small intercept of 0.04 that is not significantly different from zero with a slope of 1.19 with a 95 % confidence interval from 0.99 to 1.36. While recognizing that 1.19 is much closer to 1.1 than to 1.0, we employed two different coefficients c_{EF} for the conversion from instantaneous latent heat flux to daily latent heat flux (see Eq. 5): 1.0 as assumed in the traditional SEBAL application (Bastiaanssen et al., 1998a) and 1.1 as found by several researchers on the basis of field measurements (Brutsaert and Sugita, 1992; Anderson et al., 1997).

Figures 11 and 12 present the plots of, respectively, the adjusted (using ground measured R_n energy balance closure) sensible and latent daily heat fluxes measured at the EC towers vs. the SEBAL estimates resulting from scenarios S1–S3 with c_{EF} equals 1.1. Note there is no need for scenarios S4 and S5 since the daily net radiations measured on the ground and determined by SEBAL are very close (Table 4). For the values in Table 8, when the c_{EF} equals 1.0 the agreement is excellent for the daily latent heat fluxes (LE) with a mean MRD of 3.9 % (= (2.9 + 0.0 + 8.9)/3) but rather poor for the daily sensible heat fluxes (H) with a mean MRD of −20.4 % (= (−19.4 − 14.9 − 27.0)/3). The latter result is another demonstration how the sensible heat flux absorbs biases during the internal calibration of SEBAL. The important implication of these numbers is that using the daily sensible heat flux for calibration of SEBAL applications has a high risk of introducing severe bias. Therefore, on the basis of this study we conclude that only

HESSD
11, 13479–13539, 2014

reliable measurements of the latent heat flux, either instantaneous or daily, should be used to calibrate SEBAL and METRIC. Next, using c_{EF} value of 1.1 SEBAL estimated LEs increase, therefore MRDs (MRD = $(\overline{G} - \overline{S})/\overline{G}$) of LE decrease to be negative so that MRDs of H improve (less negative). As a result, a c_{EF} value of 1.1 leads to a better agreement for H, although inspection of only the comparison measures in Table 8 does not give us certainty which of the c_{EF} values yields more accurate estimates of H and LE. Nevertheless, the use of 1.1 is preferred in our study (non-advective conditions during months April to September) given the regression analysis presented in Fig. 10, data reported in the literature (Brutsaert and Sugita, 1992; Anderson et al., 1997), and the improved daily sensible heat fluxes by SEBAL in Table 8.

A comparison between ground measurements and SEBAL estimates of daily evapotranspiration is made in Fig. 13 where the unadjusted EC measurements of ET are compared with SEBAL estimates of ET with c_{EF} of 1.1. For scenarios S1, S2, and S3 the slopes between unadjusted ET measured at the EC tower and the SEBAL estimates are, respectively, 1.30, 1.32, and 1.08 which averages to 1.23. Thus, SEBAL ET estimates are about 21 % higher than the unadjusted ET measurements at the EC towers. This discrepancy is expected since it has been reported in the literature that the systematic underestimation of heat fluxes by the eddy covariance method can be as high as 10 to 30 % (Twine et al., 2000; Paw et al., 2004). Given the inherent uncertainties of the SEBAL approach and the eddy covariance method the agreement between the two methods is surprisingly good. Especially, considering that we compare sensible and latent heat fluxes measured in heterogeneous arid riparian areas. Therefore, this study confirms other studies (Allen et al., 2011; Bastiaanssen et al., 2005) that SEBAL is a powerful tool for high resolution mapping of evapotranspiration even where no meteorological measurements are available on the ground. This study also demonstrates that the use of SEBAL in heterogeneous landscapes such as arid riparian areas results in ET estimates that are as good as those that could be obtained using the EC method.

HESSD
11, 13479–13539, 2014

5 Conclusions

In this study we have evaluated the SEBAL extreme-condition-inverse calibration remote sensing model in arid riparian areas by comparing its predicted instantaneous and daily energy balance components with those measured on the ground with the eddy covariance method.

An analysis of differences in instantaneous R_n during late morning (Landsat overpass time) between vegetation and exposed soil emphasizes the large impact of soil in the R_n view, and the importance of proper vegetative mixture viewed by the R_n sensor. We argue that tower R_n is generally biased toward vegetation, resulting in higher R_n values. Instantaneous R_n from SEBAL, representing a larger area for heterogeneous vegetation than the net radiometer, gives lower R_n values. When these are used to close the eddy covariance energy balance, LE and H from SEBAL and LE and H from the ground based EC are much more similar. The daily net radiation values of SEBAL agree well with the ground measurements (Table 4 and Fig. 5) as expected after examination of the daily radiation balance of mixed riparian pixels in Sect. 4.2.

The instantaneous soil heat flux values of SEBAL were about 30 % higher than the ground measured values in the San Pedro and Owens Valleys (Table 6 and Fig. 6). However, this large relative difference has a relatively minor impact on the overall energy balance since its MAD of 35 $W m^{-2}$ (Table 6) hovers around 6 % percent of the SEBAL predicted instantaneous net radiation and around 5 % percent of the ground measured instantaneous net radiation. The daily G is close to zero since heat enters the soil during the day but leaves the soil during the night (Table 6). Therefore, it can be assumed in SEBAL that the daily heat flux is zero.

The instantaneous latent heat flux values of SEBAL were within −13.2 to 2.7 % of the ground measurements for the five scenarios S1–S5 (Table 7 and Fig. 9). The magnitude of these differences is similar to the variability common to eddy covariance flux measurements, i.e. it is nearly impossible to decide whether these differences are a result of bias in SEBAL or the eddy covariance method. Therefore, we conclude that

HESSD
11, 13479–13539, 2014

the SEBAL latent heat fluxes in this study over heterogeneous arid riparian areas are similar to the ones measured at the eddy covariance towers.

The instantaneous sensible heat flux values of SEBAL differ from the ground measurements by 35.0 to 47.2 % in scenarios S1, S2 and S3 but after replacing the biased ground measurement of net radiation by the SEBAL net radiation the differences reduce to 0.8 and 16.6 % for, respectively, scenarios S4 and S5. As has been explained in Sect. 4.4.1 the SEBAL sensible heat fluxes are biased since as a result of the extreme-condition-inverse internal calibration of SEBAL the sensible heat flux absorbs all biases that may occur during the SEBAL implementation.

In terms of daily sensible and latent heat fluxes, better agreement exists between ground measurements and SEBAL estimates with mean MRD's for the three scenarios range from 13.8 to −0.7 %. That is because the daily net radiations measured on the ground and determined by SEBAL agree well (Table 8 and Figs. 11 and 12). Note that the use of a multiplier on the instantaneous evaporative fraction of 1.1 to convert the instantaneous ET to daily ET is preferred for the non-advective conditions during the months April to September that were covered during this study.

An important conclusion of the comparisons between various calibration strategies for SEBAL is that ground measurements of sensible heat fluxes should be used with caution for the calibration and validation of SEBAL, since the SEBAL sensible heat flux is intentionally biased during calibration (to produce an unbiased LE) and will deviate from the ground measured sensible heat flux in order to arrive at unbiased estimates of LE.

For all five calibration scenarios, the comparison measures (r^2, MAD, RMSD and MRD) of the instantaneous and daily latent heat fluxes are strong evidence that the great strength of the SEBAL and METRIC method is its internal calibration procedure that eliminates most of the bias in latent heat flux at the expense of increased bias in sensible heat flux. We conclude that SEBAL is an effective tool for mapping actual evapotranspiration at high spatial resolutions in heterogeneous riparian areas where no high-quality hourly weather data are available.

HESSD
11, 13479–13539, 2014

Acknowledgements. The following sponsors have contributed to this study: NSF EPSCoR grant EPS-0447691; US Department of Agriculture, CSREES grant No.: 2003-35102-13654; New Mexico Universities Collaborative Research (NUCOR) program for joint research with the Los Alamos National Laboratory; and NASA New Investigator Program. The energy balance data from towers in the Middle Rio Grande Valley were provided by James Cleverly. We did our own energy balance adjustment.

References

Allen, R. G., Pereira, L. S., Raes, D., and Smith, M.: Crop evapotranspiration, FAO Irrigation drainage paper 56, FAO, Rome, 1998.

Allen, R. G., Tasumi, M., and Trezza, R.: METRIC™ Mapping Evapotranspiration at High Resolution. Applications Manual for Landsat Satellite Imagery. Version 2.0, University of Idaho, Kimberly, Idaho, 139, 2005.

Allen, R. G., Tasumi, M., and Trezza, R.: Benefits from tying satellite-based energy balance to reference evapotranspiration, Earth Observation for Vegetation Monitoring and Water Management. AIP Conference Proceedings, 852, 127–137, 10–11 November 2005, Naples (Italy), 2006.

Allen, R. G., Tasumi, M., and Trezza, R.: Satellite-based energy balance for Mapping Evapotranspiration with Internalized Calibration (METRIC) – model, J. Irrig. Drain. E.-ASCE, 133, 380–394, 2007.

Allen, R. G., Irmak, A., Trezza, R., Hendrickx, J. M. H., Bastiaanssen, W. G. M., and Kjaersgaard, J.: Satellite-based ET estimation in agriculture using SEBAL and METRIC, Hydrol. Process., 25, 4011–4027, 2011.

Anderson, M. C., Norman, J. M., Diak, G. R., Kustas, W. P., and Mecikalski., J. R.: A two-source time-integrated model for estimating surface fluxes using thermal infrared remote sensing, Remote Sens. Environ., 60, 195–216, 1997.

Arya, P. S.: Introduction to Micrometeorology, 2nd Edn., Academic Press, San Diego, 420 pp., 2001.

Bastiaanssen, W. G. M.: Regionalization of surface flux desities and moisture indicators in composite terrain: a remote sensing approach under clear skies in Mediterranean climates, Landbouwuniversiteit te Wageningen, 1995.

HESSD

11, 13479–13539, 2014

Bastiaanssen, W. G. M., Menenti, M., Feddes, R. A., and Holtslag, A. A. M.: A remote sensing surface energy balance algorithm for land (SEBAL). Part 1: Formulation, J. Hydrol., 212–213, 198–212, 1998a.

Bastiaanssen, W. G. M., Pelgrum, H., Wang, J., Ma, Y., Moreno, J. F., Roerink, G. J., Roebeling, R. A., and van der Wal, T.: A remote sensing surface energy balance algorithm for land (SEBAL). Part 2: Validation, J. Hydrol., 212–213, 213–229, 1998b.

Bastiaanssen, W. G. M.: SEBAL-based sensible and latent heat fluxes in the Irrigated Gediz Basin, Turkey, J. Hydrol., 229, 87–100, 2000.

Bastiaanssen, W. G. M., Ahmad, M.-D., and Chemin, Y.: Satellite surveillance of evaporative depletion across the Indus Basin, Water Resour. Res., 38, 1273, doi:10.1029/2001WR000386, 2002.

Bastiaanssen, W. G. M., Noordman, E. J. M., Pelgrum, H., Davids, G., Thoreson, B. P., and Allen, R. G.: SEBAL model with remotely sensed data to improve water-resources management under actual field conditions, J. Irrig. Drain. E.-ASCE, 131, 85–93, 2005.

Bastiaanssen, W. G. M., Klaasse, A., Zwart, S., Immerzeel, W., and Droogers, P.: The hydrological flow path and options for sustainable water-resources management in the overexploited Rio Bravo Basin, a world bank project, Final report, 102 pp., the Netherlands, 2006.

Brutsaert, W. and Sugita, M.: Application of self-preservation in the diurnal evolution of the surface energy budget to determine daily evaporation, J. Geophys. Res., 97, 18377–18382, 1992.

Brutsaert, W., Hsu, A. Y., and Schmugge, T. J.: Parameterization of surface heat fluxes above a forest with satellite thermal sensing and boundary layer soundings, J. Appl. Meteorol., 32, 909–917, 1993.

Campbell, G. S. and Norman, J. M.: An Introduction to Environmental Biophysics, 2nd edn., Springer, New York, NY, 286 pp., 1998.

Choi, M., Kustas, W. P., Anderson, M. C., Allen, R. G., Li, F., and Kjaersgaard, J. H.: An intercomparison of three remote sensing-based surface energy balance algorithms over a corn and soybean production region (Iowa, US) during SMACEX, Agr. Forest Meteorol., 149, 2082–2097, 2009.

Choudhury, B. J., Reginato, R. J., and Idso, S. B.: An analysis of infrared temperature observations over wheat and calculation of latent heat flux, Agr. Forest Meteorol., 37, 75–88, 1986.

HESSD
11, 13479–13539, 2014

Choudhury, B. J.: Estimating evaporation and carbon assimilation using infrared temperature data: vistas in modeling, in: Theory and Application of Remote Sensing, edited by: Asrar, G., Wiley, New York, 628–690, 1989.

Cleverly, J. R., Dahm, C. N., Thibault, J. R., Gilroy, D. J., and Coonrod, J. E. A.: Seasonal estimates of actual evapo-transpiration from Tamarix ramosissima stands using three-dimensional eddy covariance, J. Arid Environ., 52, 181–197 doi:10.1006/jare.2002.0972, 2002.

Cosgrove, B. A., Lohmann, D., Mitchell, K. E., Houser, P. R., Wood, E. F., Schaake, J., Robock, A., Marshall, C., Sheffield, J., Luo, L., Duan, Q., Pinker, R. T., Tarpley, J. D., Higgins, R. W., and Meng, J.: Real-time and retrospective forcing in the North American Land Data Assimilation System (NLDAS) project, J. Geophys. Res., 108, 8842, doi:10.1029/2002JD003118, 2003.

Costigan, K. R., Bossert, J. E., and Langley, D. L.: Atmospheric/hydrologic models for the Rio Grande Basin: simulations of precipitation variability, Global Planet. Change, 25, 83–110, 2000.

Crago, R. D.: Conservation and variability of the evaporative fraction during the daytime, J. Hydrol., 180, 173–194, 1996.

De Bruin, H. A. R.: From Penman to Makkink, in: Evaporation and Weather. Proceedings and Information No. 39, edited by: Hooghart, J. C., TNO Committee on Hydrological Research, The Hague, 5–31, 1987.

De Bruin, H. A. R., Bink, N. J., and Kroon, L. J. M.: Fluxes in the surface layer under advective conditions, in: Land Surface Evaporation, edited by: Schmugge, T. J. and Andre, J.-C., Springer-Verlag New York, Inc., 1991.

Droogers, P. and Allen, R. G.: Estimating reference evapotranspiration under inaccurate data conditions, Irrig. Drain. Syst., 16, 33–45, 2002.

Du, J., Song, K., Wang, Z., Zhang, B., and Liu, D.: Evapotranspiration estimation based on MODIS products and Surface Energy Balance Algorithms for Land (SEBAL) model in Sanjiang Plain, Northeast China, Chinese Geogr. Sci., 23, 73–91, 2013.

Elmore, A. J., Mustard, J. F., and Manning, S. J.: Regional patterns of plant community response to changes in water: Owens Valley, California., Ecol. Appl., 13, 443–460, 2002.

Farah, H. O., Bastiaanssen, W. G. M., and Feddes, R. A.: Evaluation of the temporal variability of the evaporative fraction in a tropical watershed, Int. J. Appl. Earth Obs., 5, 129–140, 2004.

HESSD
11, 13479–13539, 2014

Field, R. T., Fritschen, L. J., Kanemasu, E. T., Smith, E. A., Stewart, J. B., Verma, S. B., and Kustas, W. B.: Calibration, comparison and correction of net radiation instruments used during FIFE, J. Geophys. Res., 97, 18681–18695, 1992.

Fox, D. G.: Judging air quality model performance: a summary of the AMS Workshop on Dispersion Model Performance, B. Am. Meteorol. Soc., 62, 599–609, 1981.

Franks, S. W. and Beven, K. J.: Estimation of evapotranspiration at the landscape scale: a fuzzy disaggregation approach, Water Resour. Res., 33, 2929–2938, 1997.

Fuchs, M. and Hadas, A.: Analysis and performance of an improved soil heat flux transducer, Soil Sci. Soc. Am. Pro., 37, 173–175, 1973.

Gash, J. H. C.: A note on estimating the effect of a limited fetch on micrometeorological evaporation measurements, Bound.-Lay. Meteorol., 35, 409–413, 1986.

Gibson, L. A., Jarmain, C., Su, Z., and Eckardt, F.: Review: estimating evapotranspiration using remote sensing and the surface energy balance system – a South African perspective, Water SA, 39, 477–483, 2013.

Granger, R. J.: Satellite-derived estimates of evapotranspiration in the Gediz basin, J. Hydrol., 229, 70–76, 2000.

Hall, F. G., Huemmrich, K. F., Goetz, S. J., Sellers, P. J., and Nickeson, J. E.: Satellite remote sensing of surface energy balance: sucesses, failures, and unresolved issues in FIFE, J. Geophys. Res., 97, 19061–19089, 1992.

Halldin, S. and Lundroth, A.: Errors in net radiometry: comparison and evaluation of six radiometer designs, J. Atmos. Ocean. Tech., 6, 762–783, 1992.

Hemakumara, H., Chandrapala, L., and Moene, A.: Evapotranspiration fluxes over mixed vegetation areas measured from a large aperture scintillometer, Agr. Water Manage., 58, 109–122, 2003.

Hendrickx, J. M. H., Vink, N. H., and Fayinke, T.: Water requirement for irrigated rice in a semi-arid region in West Africa, Agr. Water Manage., 11, 75–90, 1986.

Hong, S.-H.: Mapping regional distributions of energy balance components using optical remotely sensed imagery, Ph.D. thesis, New Mexico Institute of Mining and Technology, Socorro, NM, 378 pp., 2008.

Horst, T. W. and Weil, J. C.: Footprint estimation for scalar flux measurements in the atmospheric surface layer, Bound.-Lay. Meteorol., 59, 279–296, 1992.

HESSD
11, 13479–13539, 2014

Hsieh, C.-I., Katul, G. G., and Chi, T.-W.: An approximate analytical model for footprint estimation of scalar fluxes in thermally stratified atmospheric flows, Adv. Water Resour., 23, 765–772, 2000.

Humes, K. S., Kustas, W. P., Moran, M. S., Nichols, W. D., and Weltz, M. A.: Variability of emissivity and surface temperature over a sparsely vegetated surface, Water Resour. Res., 30, 1299–1310, 1994.

Jacob, F., Olioso, A., Gu, X. F., Su, Z., and Seguin, B.: Mapping surface fluxes using airborne visible, near infrared, thermal infrared remote sensing data and a spatialized surface energy balance model, Agronomie, 22, 669–680, doi:10.1051/agro:2002053, 2002.

Jiang, L. and Islam, S.: Estimation of surface evaporation map over southern Great Plains using remote sensing data, Water Resour. Res., 37, 329–340, 2001.

Kite, G. W. and Droogers, P.: Comparing evapotranspiration estimates from satellites, hydological models and field data, J. Hydrol., 229, 3–18, 2000.

Kizer, M. A. and Elliott, R. L.: Eddy correlation systems for measuring evapotranspiration, T. ASAE, 34, 387–392, 1991.

Kleissl, J., Gomez, J. D., Hong, S.-H., and Hendrickx, J. M. H.: Large aperture scintillometer intercomparison study, Bound.-Lay. Meteorol., 128, 133–150, 2008.

Kleissl, J., Hong, S.-H., and Hendrickx, J. M. H.: New Mexico scintillometer network. Supporting remote sensing and hydrologic and meteorological models, B. Am. Meteorol. Soc., 90, 207–218, 2009.

Kurc, S. A. and Small, E. E.: Dynamics of evapotranspiration in semiarid grassland and shrubland ecosystems during the summer monsoon season, central New Mexico, Water Resour. Res., 40, W09305, doi:10.1029/2004WR003068, 2004.

Kustas, W. P. and Norman, J. M.: Use of remote sensing for evapotranspiration monitoring over land surfaces, Hydrolog. Sci. J., 41, 495–516, 1996.

Kustas, W. P., Prueger, J. H., Hatfield, J. L., Ramalingam, K., and Hipps, L. E.: Variability in soil heat flux from a mesquite dune site, Agr. Forest Meteorol., 103, 249–264, 2000.

Loescher, H. W., Ocheltree, T., Tanner, B., Swiatek, E., Dano, B., Wong, J., Zimmerman, G., Campbell, J., Stock, C., Jacobsen, L., Shiga, Y., Kollas, J., Liburdy, J., and Law, B. E.: Comparison of temperature and wind statistics in contrasting environments among different sonic anemometer-thermometers, Agr. Forest Meteorol., 133, 119–139, 2005.

HESSD
11, 13479–13539, 2014

Ma, Y., Menenti, M., Tsukamoto, O., Ishikawa, H., Wang, J., and Gao., Q.: Remote sensing parameterization of regional land surface heat fluxes over arid area in northwestern China, J. Arid Environ., 57, 257–273, 2004.
Moran, M. S. and Jackson, R. B.: Assessing the spatial distribution of evapotranspiration using remotely sensed inputs, J. Environ. Qual., 20, 725–735, 1991.
Mu, Q., Zhao, M., and Running, S. W.: Improvements to a MODIS global terrestrial evapotranspiration algorithm, Remote Sens. Environ., 115, 1781–1800, 2011.
Norman, J. M., Kustas, W. P., and Humes, K. S.: A two-source approach for estimating soil and vegetation energy fluxes from observations of directional radiometric surface temperature, Agr. Forest Meteorol., 77, 263–293, 1995.
Norman, J. M., Anderson, M. C., Kustas, W. P., French, A. N., Mecikalski, J., Torn, R., Diak, G. R., Schmugge, T. J., and Tanner, B. C. W.: Remote sensing of surface energy fluxes at 10^1-m pixel resolutions, Water Resour. Res., 39, 1221, doi:10.1029/2002WR001775, 2003.
Parlange, M. B., Eichinger, W. E., and Albertson, J. D.: Regional scale evaporation and the atmosphere boundary layer, Rev. Geophys., 33, 99–124, 1995.
Paw, K. T., Wharton, S., Xu, L., Falk, M., Schroeder, M., and Gonzales, E.: Zen and the art of energy balance closure, Symposium "Progress in Radiation and Energy Balance Closure", 68th Annual Meeting Soil Science Society of America, Seattle, Washington, 31 October–4 November 2004.
Pelgrum, H. and Bastiaanssen, W. G. M.: An intercomparison of techniques to determine the area-averaged latent heat flux from individual in situ observations: a remote sensing approach using the European Field Experiment in a Desertification-Threatened Area data, Water Resour. Res., 32, 2775–2786, 1996.
Peters Lidard, C. D., Kumar, S., Tian, Y., Eastman, J. L., and Houser, P.: Global urban-scale land–atmosphere modeling with the land information system, 84th AMS Annual Meeting, Symposium on Planning, Nowcasting, and Forecasting in the Urban Zone, 84th AMS Annual Meeting, 11–15 January 2004, Seattle, Washington, 2004.
Sauer, T. J.: Soil heat flux, in: Encyclopedia of Soil Science, edited by: Lal, R., Marcel Dekker Inc., New York, NY, 647–649, 2002a.
Sauer, T. J.: Heat flux density, in: Methods of Soil Analysis. Part 1, edited by: Dane, J. and Topp, C., Soil Science Society of America Madison, Wisconsin, 1233–1248, 2002b.

HESSD
11, 13479–13539, 2014

Sauer, T. J., Meek, D. W., Ochsner, T. E., Harris, A. R., and Horton, R.: Errors in heat flux measurement by flux plates of contrasting design and thermal conductivity, Vadose Zone J., 2, 580–588, 2003.

Schmid, H. P. and Oke, T. R.: A model to estimation the source area contributing to turbulent exchange in the surface layer over patchy terrain, Q. J. Roy. Meteor. Soc., 116, 965–988, 1990.

Schuepp, P. H., Leclerc, M. Y., MacPherson, J. I., and Desjardins, R. L.: Footprint prediction of scalar fluxes from analytical solutions of the diffusion equation, Bound.-Lay. Meteorol., 50, 355–373, 1990.

Schüttemeyer, D., Schillings, C., Moene, A. F., and Bruin, H. A. R. D.: Satellite-based actual evapotranspiration over drying semiarid terrain in West Africa, J. Appl. Meteorol. Clim., 46, 97–111 doi:10.1175/JAM2444.1, 2007.

Scott, R. L., Shuttleworth, J. W., Goodrich, D. C., and Maddock III, T.: The water use of two dominant vegetation communities in a semiarid riparian ecosystem, Agr. Forest Meteorol., 105, 241–256, 2000.

Scott, R. L., Edwards, E. A., Shuttleworth, W. J., Huxman, T. E., Watts, C., and Goodrich, D. C.: Interannual and seasonal variation in fluxes of water and carbon dioxide from a riparian woodland ecosystem, Agr. Forest Meteorol., 122, 65–84, 2004.

Seguin, B. D. and Itier, B.: Using midday surface temperature to estimate daily evapotranspiration from satellite thermal IR data, Int. J. Remote Sens., 4, 371–383, 1983.

Senay, G. B., Bohms, S., Singh, R. K., Gowda, P. H., Velpuri, N. M., Alemu, H., and Verdin, J. P.: Operational evapotranspiration mapping using remote sensing and weather datasets: a new parameterization for the SSEB approach, J. Am. Water Resour. As., 49, 577–591, 2013.

Stannard, D. I.: Comparison of Penman–Monteith, Shuttleworth-Wallace, and Modified Priestley-Tayor evapotranspiration models for wildland vegetation in semiarid rangeland, Water Resour. Res., 29, 1379–1392, 1993.

Steinwand, A. L., Harrington, R. F., and Or, D.: Water balance for Great Basin phreatophytes derived from eddy covariance, soil water, and water table measurements, J. Hydrol., 329, 595–605, 2006.

Stromberg, J. C.: Dynamics of Fremont cottonwood (*Populus fremontii*) and saltcedar (*Tamarix chinensis*) populations along the San Pedro River, Arizona, J. Arid Environ., 40, 133–155, 1998.

HESSD
11, 13479–13539, 2014

Su, Z.: The Surface Energy Balance System (SEBS) for estimation of turbulent heat fluxes, Hydrol. Earth Syst. Sci., 6, 85–100, doi:10.5194/hess-6-85-2002, 2002.
Sugita, M. and Brutsaert, W.: Daily evaporation over a region from lower boundary layer profiles measured with radiosondes, Water Resour. Res., 27, 747–752, 1991.
Sumner, D. M. and Jacobs, J. M.: Utility of Penman–Monteith, Priestley–Taylor, reference evapotranspiration, and pan evaporation methods to estimate pasture evapotranspiration, J. Hydrol., 308, 81–104, 2005.
Tasumi, M.: Progress in operational estimation of regional evapotranspiration using satellite imagery, PhD thesis, University of Idaho, Moscow, Idaho, 2003.
Teixeira, A. H. C., Bastiaanssen, W. G. M., Moura, M. S. B., Soares, J. M., Ahmad, M. D., and Bos, M. G.: Energy and water balance measurements for water productivity analysis in irrigated mango trees, Northeast Brazil, Agr. Forest Meteorol., 148, 1524–1537, 2008.
Trezza, R.: Evapotranspiration using a satellite-based surface energy balance with standardized ground control. Ph.D. thesis, Utah State University, Logan, Utah, 2002.
Twine, T. E., Kustas, W. P., Norman, J. M., Cook, D. R., Houser, P. R., Meyers, T. P., Prueger, J. H., Starks, P. J., and Wesely, M. L.: Correcting eddy-covariance flux underestimates over a grassland, Agr. Forest Meteorol., 103, 279–300, 2000.
Wang, J., Bastiaanssen, W. G. M., Ma, Y., and Pelgrum, H.: Aggregation of land surface parameters in the oasis-desert systems of Northwest China, Hydrol. Process., 12, 2133–2147, 1998.
Willmott, C. J.: On the validation of models, Phys. Geogr., 2, 184–194, 1981.
Willmott, C. J.: Some comments on the evaluation of model performance, B. Am. Meteorol. Soc., 63, 1309–1313, 1982.
Willmott, C. J. and Wicks, D. E.: An empirical method for the spatial interpolation of monthly precipitation within California, Phys. Geogr., 1, 59–73, 1980.
Wright, J. L.: New evapotranspiration crop coefficients, J. Irrig. Drain. E.-ASCE, 108, 57–74, 1982.
Yang, Y. T. and Shang, S. H.: A hybrid dual source scheme and trapezoid framework based evapotranspiration model (HTEM) using satellite images: algorithm and model test, J. Geophys. Res., 118, 2284–2300, 2013.
Zwart, S. J. and Leclert, L. M. C.: A remote sensing-based irrigation performance assessment: a case study of the Office du Niger in Mali, Irrigation Sci., 28, 371–385, 2010.

HESSD
11, 13479–13539, 2014

Table 1. List of Landsat 7 ETM+ images used in this study (overpass around 10:30 a.m.).

Area	Date	Path/Row
Rio Grande	7 Apr 2000	33/36
Rio Grande	28 Jul 2000	33/36
Rio Grande	14 Sep 2000	33/36
Rio Grande	30 Sep 2000	33/36
Rio Grande	9 May 2000	33/36
Rio Grande	4 Jun 2001	34/36
Rio Grande	6 May 2002	34/36
Rio Grande	31 May 2002	33/36
Rio Grande	31 May 2002	33/37
Rio Grande	16 Jun 2002	33/36
Rio Grande	19 Aug 2002	33/36
Owens Valley	10 Jul 2002	41/34
Owens Valley	11 Aug 2002	41/34
Owens Valley	12 Sep 2002	41/34
San Pedro	16 May 2003	35/38
San Pedro	12 Aug 2003	35/38

HESSD
11, 13479–13539, 2014

Table 2. Site characteristics and sensor heights on the eddy covariance towers.

Site	Longitude/Latitude	Vegetation type	Elevation (m)	Vegetation height (m)	Sensor height (m)
Rio Grande – BDAS	106.88° W/33.78° N	saltcedar	1370	6.2	8.2
Rio Grande – BLN	106.75° W/34.59° N	cottonwood	1460	25.1	27.2
Rio Grande – SEV	106.87° W/34.27° N	saltcedar	1430	4.9	6.5
Rio Grande – SHK	106.68° W/34.96° N	cottonwood	1500	23.7	26.3
Owens – FSL138	118.43° W/37.41° N	alkali meadow	1280	0.2	2.5
Owens – PLC018	118.35° W/37.37° N	rabbitbrush scrub	1250	0.5	2.5
Owens – PLC074	118.36° W/37.32° N	saltbush meadow	1240	1.0	2.5
Owens – PLC185	118.33° W/37.27° N	desert sink scrub	1220	0.5	2.5
Owens – BLK100	118.24° W/36.90° N	alkali meadow	1170	0.2	2.5
San Pedro – CM	110.18° W/31.66° N	mesquite	1190	7.0	14
San Pedro – LSS	110.14° W/31.56° N	sacaton	1230	1.0	3.5
San Pedro – LSM	110.13° W/31.57° N	mesquite	1240	3.5	6.5

HESSD
11, 13479–13539, 2014

Table 3. Scenarios of comparison between SEBAL estimates and ground measurements of net radiation R_n, soil heat flux G, and sensible and latent heat fluxes H and LE.

ID	Scenario	R_n Used for Energy Balance Closure
S1	EC Approach (EC_FP)[a]	Ground Measured R_n
S2	EC Approach (EC_TP)[b]	Ground Measured R_n
S3	EM Approach[c]	Ground Measured R_n
S4	EC Approach (EC_TP/SR_n)[d]	SEBAL Estimated R_n
S5	EM Approach (SR_n)[e]	SEBAL Estimated R_n

[a] Hot pixel selected by matching the ground measured instantaneous LE (adjusted for closure error using the ground measured R_n) at satellite overpass with the **footprint weighted averaged SEBAL LE**. SEBAL LE compared against ground measured instantaneous LE (adjusted for closure error using the ground measured R_n) at satellite overpass.

[b] Hot pixel selected by matching the ground measured instantaneous LE (adjusted for closure error using the ground measured R_n) at satellite overpass with the **SEBAL LE at the tower pixel**. SEBAL LE compared against ground measured instantaneous LE (adjusted for closure error using the ground measured R_n) at satellite overpass.

[c] Hot pixel selected by the empirical approach **without use of ground measurements**. SEBAL LE is compared against ground measured instantaneous LE (adjusted for closure error using the ground measured R_n) at satellite overpass.

[d] Hot pixel selected by matching the ground measured instantaneous LE (adjusted for closure error using the ground measured R_n) at satellite overpass with the **SEBAL LE at the tower pixel**. SEBAL LE compared against ground measured instantaneous LE (adjusted for closure error using the SEBAL estimated R_n) at satellite overpass.

[e] Hot pixel selected by the empirical approach **without use of ground measurements**. SEBAL LE is compared against ground measured instantaneous LE (adjusted for closure error using the SEBAL estimated R_n) at satellite overpass.

HESSD
11, 13479–13539, 2014

Table 4. Quantitative measures for comparison of SEBAL instantaneous and daily net radiation estimates ($\overline{S}$) vs. ground measurements ($\overline{G}$) using the EC and Empirical Approaches for selection of hot and cold pixels.

Selection Cold and Hot Pixel	n	$\overline{G}$	$\overline{S}^{d}$	SD_G	SD_S	r^2	MAD	RMSD	MRD
Instantaneous R_n	(–)	($W m^{-2}$)	($W m^{-2}$)	($W m^{-2}$)	($W m^{-2}$)	(–)	($W m^{-2}$)	($W m^{-2}$)	%
S1 – EC Approach (FP^a)	25	654	569	86	90	0.56	88	105	13.0
S2 – EC Approach (TP^b)	25	654	571	86	89	0.56	87	103	12.8
S3 – Empirical Approach	25	654	559	86	88	0.56	97	113	14.6
Daily R_n	(–)	($MJ m^{-2} day^{-1}$)	($MJ m^{-2} day^{-1}$)	($MJ m^{-2} day^{-1}$)	($MJ m^{-2} day^{-1}$)	(–)	($MJ m^{-2} day^{-1}$)	($MJ m^{-2} day^{-1}$)	%
S1/S2 – EC Approach[c]	24	15.6	16.0	3.1	3.1	0.75	1.3	1.6	−2.9
S3 – Empirical Approach	24	15.6	15.9	3.1	3.0	0.69	1.3	1.8	−2.3

[a] Cold and hot pixels were selected by matching the instantaneous LE measured at the EC tower with the footprint weighted averaged SEBAL instantaneous LE.
[b] Cold and hot pixels were selected by matching the instantaneous LE measured at the EC tower with the SEBAL instantaneous LE of the EC tower pixel.
[c] The daily R_n does not depend on the selection of the cold and hot pixels; both EC approaches yield the same values. [d]The SEBAL instantaneous R_n estimate ($\overline{S}$) was obtained by calculating the footprint weighted average for the instantaneous R_n; the daily R_n ($\overline{S}$) was obtained as the average SEBAL daily R_n of the 25 pixels around the EC tower.

HESSD
11, 13479–13539, 2014

Table 5. Selected instantaneous and daily net radiation fluxes and relevant parameters for adjacent clusters of vegetated and bare soil pixels on 16 June 2002.

Vegetation	Albedo (–)		NDVI[a] (–)		T_s (K)		Instantaneous Net Radiation ($W m^{-2}$)			Daily NetRadiation ($MJ m^{-2} day^{-1}$)			N[b]
	Veg	Bare	Veg	Bare	Veg	Bare	Veg	Bare	Ratio	Veg	Bare	Ratio	
Alfalfa	0.22	0.32	0.84	0.14	299	325	634	384	1.65	17.9	14.8	1.21	50
Alfalfa	0.21	0.31	0.80	0.24	301	322	627	408	1.54	18.1	15.1	1.20	20
saltcedar	0.16	0.32	0.65	0.14	302	326	670	379	1.77	19.8	14.8	1.34	50
saltcedar	0.14	0.31	0.49	0.24	308	322	657	408	1.61	20.6	15.1	1.36	20

[a] NDVI = Normalized Difference Vegetation Index.
[b] N = number of pixels in each.

HESSD
11, 13479–13539, 2014

Table 6. Quantitative measures for comparison of instantaneous and daily SEBAL soil heat flux estimates ($\overline{S}$) vs. ground measurements ($\overline{G}$) using the EC and Empirical Approaches for selection of hot and cold pixels.

Selection Cold and Hot Pixel	N^{d}	$\overline{G}$	$\overline{S}^{e}$	SD_G	SD_S	r^2	MAD	RMSD	MRD
Instantaneous G	(–)	($W m^{-2}$)	($W m^{-2}$)	($W m^{-2}$)	($W m^{-2}$)	(–)	($W m^{-2}$)	($W m^{-2}$)	%
EC Approach (FP^{a})	6	76	101	26	13	0.02	35	35	−32.2
EC Approach (TP^{b})	6	76	101	26	13	0.02	35	35	−31.9
Empirical Approach	6	76	100	26	13	0.02	34	34	−30.9
Daily G	(–)	($MJ m^{-2} day^{-1}$)	($MJ m^{-2} day^{-1}$)	($MJ m^{-2} day^{-1}$)	($MJ m^{-2} day^{-1}$)	(–)	($MJ m^{-2} day^{-1}$)	($MJ m^{-2} day^{-1}$)	%
EC Approach[c]	24	0.5	0.0	0.4	0.0	–	0.5	0.6	> 100
Empirical Approach	24	0.5	0.0	0.4	0.0	–	0.5	0.6	> 100

[a] Cold and hot pixels were selected by matching the instantaneous LE measured at the EC tower with the footprint weighted averaged SEBAL instantaneous LE.
[b] Cold and hot pixels were selected by matching the instantaneous LE measured at the EC tower with the SEBAL instantaneous LE of the EC tower pixel.
[c] The daily soil heat flux does not depend on the selection of the cold and hot pixels; both EC Approaches yield the same values.
[d] No instantaneous soil heat flux measurements were available in the Middle Rio Grande Basin.
[e] The SEBAL instantaneous soil heat flux estimate ($\overline{S}$) was obtained by calculating the footprint average for the instantaneous soil heat flux; the daily soil heat flux ($\overline{S}$) was obtained as the average SEBAL daily soil heat flux of the 25 pixels around the EC tow.

HESSD
11, 13479–13539, 2014

Table 7. Quantitative measures for comparison of SEBAL derived instantaneous sensible (H) and latent (LE) heat fluxes estimates ($\overline{S}$) vs. ground measurements ($\overline{G}$).

Scenario	Selection Anchor Pixel	Comments		n	$\overline{G}^{f}$	$\overline{S}^{g}$	SD_G	SD_S	r^2	MAD	RMSD	MRD
				(–)	(Wm^{-2})	(Wm^{-2})	(Wm^{-2})	(Wm^{-2})	(–)	(Wm^{-2})	(Wm^{-2})	%
S1	EC Approach (FP)[a]	–	H	25	262	156	151	105	0.76	108	131	40.4
			LE	25	299	314	174	170	0.90	39	57	−5.0
S2	EC Approach (TP)[b]	–	H	25	262	138	151	91	0.81	126	147	47.2
			LE	25	299	333	174	162	0.85	56	74	−11.5
S3	EM Approach	–	H	25	262	171	151	77	0.64	111	135	35.0
			LE	25	299	291	174	143	0.78	66	81	2.7
S4	EC Approach (TP)[c]	SEBAL R_n replaces ground R_n[d]	H	25	209	207	112	114	0.83	36	46	0.8
			LE	25	262	258	171	170	0.92	39	48	1.7
S5	EM Approach	SEBAL R_n replaces ground R_n[e]	H	25	205	171	110	77	0.59	61	77	16.6
			LE	25	257	291	167	143	0.82	61	77	−13.2

[a] Anchor pixels were selected by matching the instantaneous LE at the satellite overpass measured at the EC tower and the footprint weighted averaged SEBAL flux.
[b] Anchor pixels were selected by matching the instantaneous LE at the satellite overpass measured at the EC tower and the SEBAL flux of the tower pixel.
[c] Anchor pixels were selected by matching the instantaneous LE at the satellite overpass measured at the EC tower and the SEBAL flux of the tower pixel. In S4, the SEBAL estimated R_n replaces the R_n measured on the ground for adjustment of the latent heat flux.
[d] Instead of using the R_n measurements made on the ground, the SEBAL derived R_n in Scenario 2 is used for the determination of the ground measured energy balance and in adjusting the H and LE from the EC for closure error (using Bowen ratio).
[e] Instead of using the R_n measurements made on the ground, the SEBAL derived R_n in Scenario 3 is used for the determination of the ground measured energy balance and in adjusting the H and LE from the EC for closure error (using Bowen ratio).
[f] The heat fluxes have been calculated from the EC measurements. Since no soil heat flux measurements were available for the Middle Rio Grande Basin, the SEBAL soil heat flux was used to establish the ground measured energy balance.
[g] The SEBAL estimates of the instantaneous H and LE were obtained by calculating the footprint weighted averaged SEBAL heat fluxes.

HESSD
11, 13479–13539, 2014

Table 8. Quantitative measures for comparison of SEBAL derived daily sensible (H) and latent (LE) heat fluxes estimates ($\overline{S}$) vs. ground measurements ($\overline{G}$).

$EF_{24} = 1.0 \times EF_{inst}$											
Scenario	Selection Anchor Pixel		n	$\overline{G}^f$	$\overline{S}^g$	SD_G	SD_S	r^2	MAD	RMSD	MRD
			(–)	$MJ\,m^{-2}\,day^{-1}$	$MJ\,m^{-2}\,day^{-1}$	$MJ\,m^{-2}\,day^{-1}$	$MJ\,m^{-2}\,day^{-1}$	(–)	$MJ\,m^{-2}\,day^{-1}$	$MJ\,m^{-2}\,day^{-1}$	%
S1	EC Approach (FP)[a]	H	24	6.0	7.2	3.7	3.2	0.41	2.3	3.1	−19.4
		LE	24	9.1	8.9	4.4	4.9	0.78	1.7	2.2	2.9
S2	EC Approach (TP)[b]	H	24	6.0	6.9	3.7	3.3	0.32	2.6	3.3	−14.9
		LE	24	9.1	9.1	4.4	5.0	0.72	2.2	2.6	0.0
S3	EM Approach	H	24	6.0	7.6	3.7	2.7	0.37	2.6	3.3	−27.0
		LE	24	9.1	8.3	4.4	4.2	0.69	1.9	2.6	8.9
$EF_{24} = 1.1 \times EF_{inst}$											
Scenario	Selection Anchor Pixel		n	$\overline{G}^f$	$\overline{S}^g$	SD_G	SD_S	r^2	MAD	RMSD	MRD
			(–)	$MJ\,m^{-2}\,day^{-1}$	$MJ\,m^{-2}\,day^{-1}$	$MJ\,m^{-2}\,day^{-1}$	$MJ\,m^{-2}\,day^{-1}$	(–)	$MJ\,m^{-2}\,day^{-1}$	$MJ\,m^{-2}\,day^{-1}$	%
S1	EC Approach (FP)[a]	H	24	6.0	6.3	3.7	3.5	0.41	2.1	3.0	−5.6
		LE	24	9.1	9.7	4.4	5.3	0.78	1.9	2.5	−6.3
S2	EC Approach (TP)[b]	H	24	6.0	6.0	3.7	3.6	0.32	2.7	3.3	−0.8
		LE	24	9.1	10.0	4.4	5.4	0.71	2.4	3.0	−9.3
S3	EM Approach	H	24	6.0	6.9	3.7	3.0	0.42	2.3	2.9	−14.8
		LE	24	9.1	9.2	4.4	4.6	0.69	2.0	2.5	−0.3

[a] Anchor pixels were selected by matching the instantaneous LE at the satellite overpass measured at the EC tower and the footprint weighted averaged SEBAL flux.
[b] Anchor pixels were selected by matching the instantaneous LE at the satellite overpass measured at the EC tower and the SEBAL flux of the tower pixel.
[e] Instead of using the R_n measurements made on the ground, the SEBAL derived R_n in Scenario 3 is used for the determination of the ground measured energy balance.
[f] The heat fluxes have been calculated from the EC measurements. Since no soil heat flux measurements were available for the Middle Rio Grande Basin, the SEBAL soil heat flux was used to establish the ground measured energy balance.
[g] The SEBAL estimates of the instantaneous H and LE were obtained by calculating the footprint weighted averaged SEBAL heat fluxes.

HESSD
11, 13479–13539, 2014

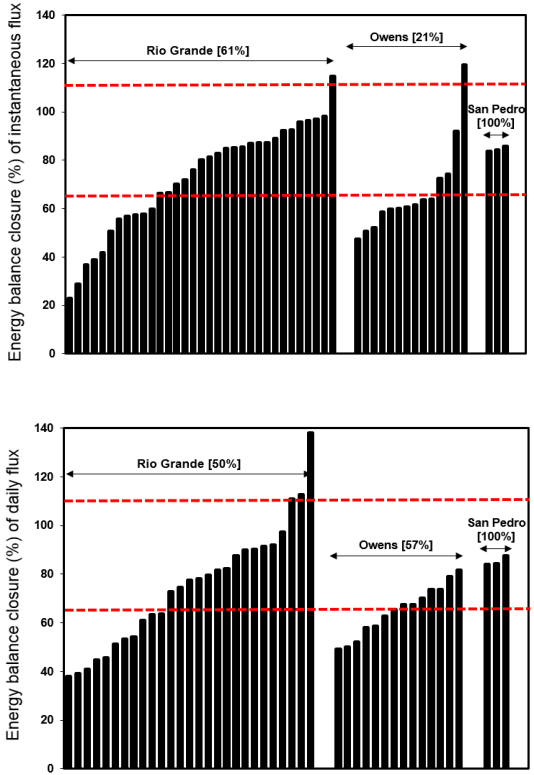

Figure 1. Distribution of energy balance relative closure $(H + \mathrm{LE})/(R_n - G)$ of instantaneous (top panel) and total daily (bottom panel) fluxes from eddy covariance towers. Each "bar" represents a satellite overpass day. The dotted lines show criteria of acceptable closure (65 and 110 %) and percentage of the data having acceptable closure is shown in bracket.

HESSD
11, 13479–13539, 2014

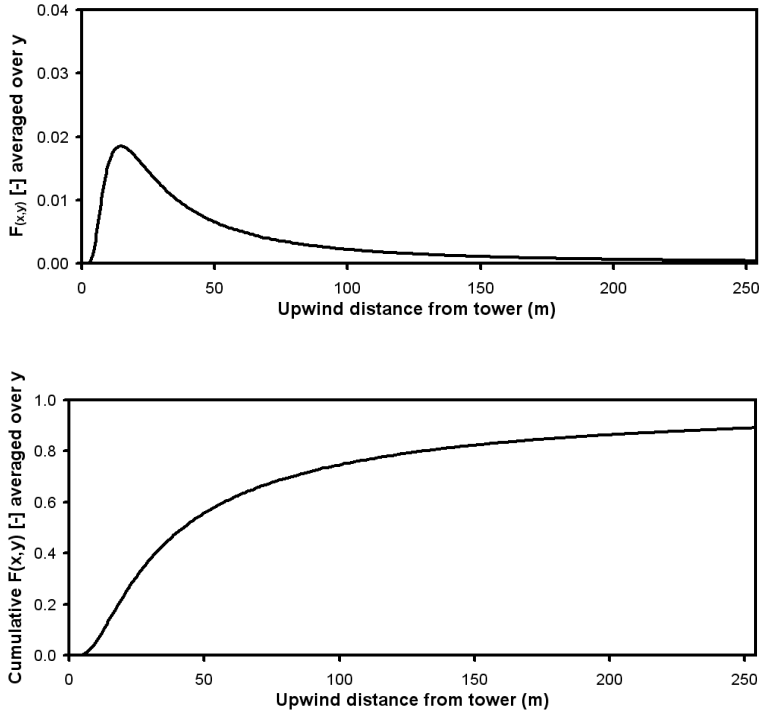

Figure 2. Footprint size and footprint intensity from the eddy covariance tower located at SEV (saltcedar) in Rio Grande on 19 August 2002 (10:40 a.m.) (wind speed: 3.4 m s^{-1}, vegetation height: 4.9 m and sonic anemometer height from ground: 6.5 m).

HESSD
11, 13479–13539, 2014

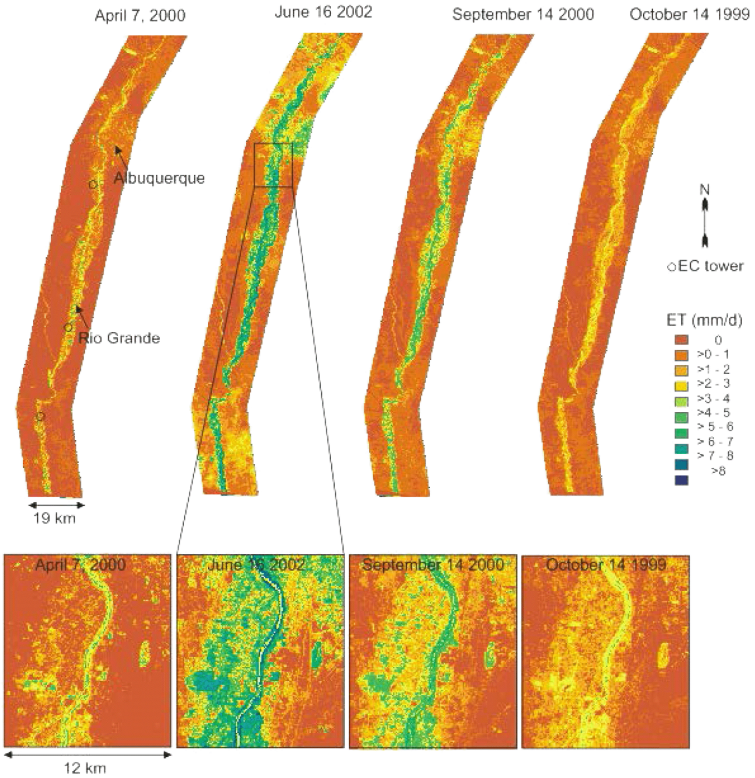

Figure 3. SEBAL daily evapotranspiration (mm day^{-1}) maps along the Rio Grande in spring, summer and fall.

HESSD
11, 13479–13539, 2014

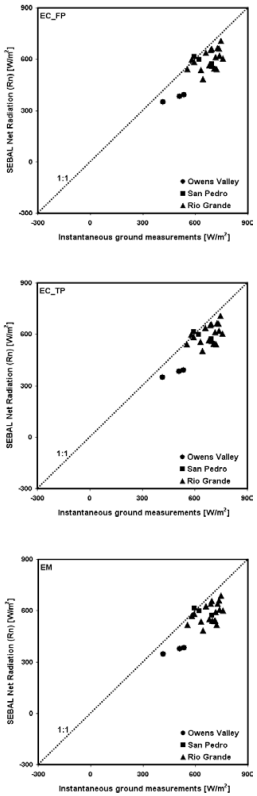

Figure 4. Comparison of instantaneous net radiation (R_n) between net radiometer measurements and SEBAL estimates. EC_FP (S1) method selected anchor pixels to match fluxes of the ground measured instantaneous LE (adjusted for closure error) at the satellite overpass and the footprint weight averaged SEBAL LE. EC_TP (S2) method selected anchor pixels to match fluxes of the ground measured instantaneous LE and the flux of the tower pixel. EM (S3) method selected the anchor pixels with the hydrogeological features of the landscape and micrometeorological considerations.

HESSD
11, 13479–13539, 2014

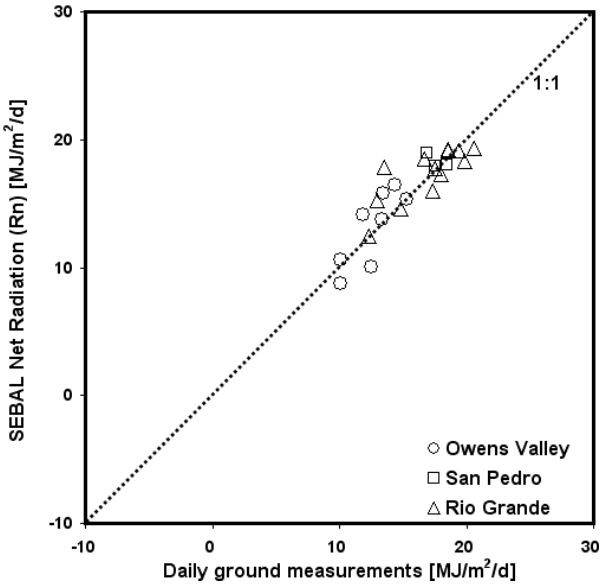

Figure 5. Comparison of daily net radiation (R_n) between net radiometer measurements and SEBAL estimates.

HESSD
11, 13479–13539, 2014

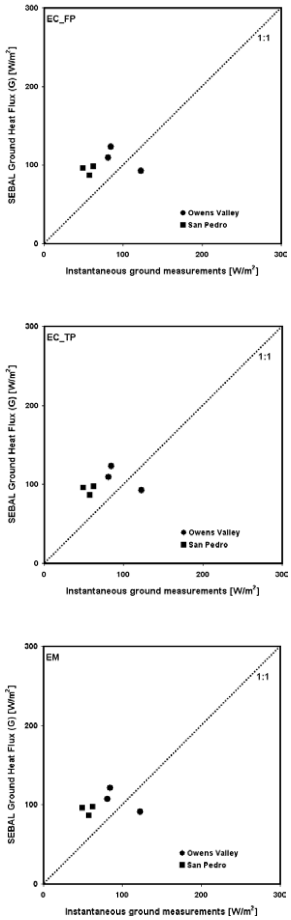

Figure 6. Comparison of instantaneous ground heat flux (G) between soil heat flux plate measurements and SEBAL estimates in Owens Valley and San Pedro Valley.

HESSD
11, 13479–13539, 2014

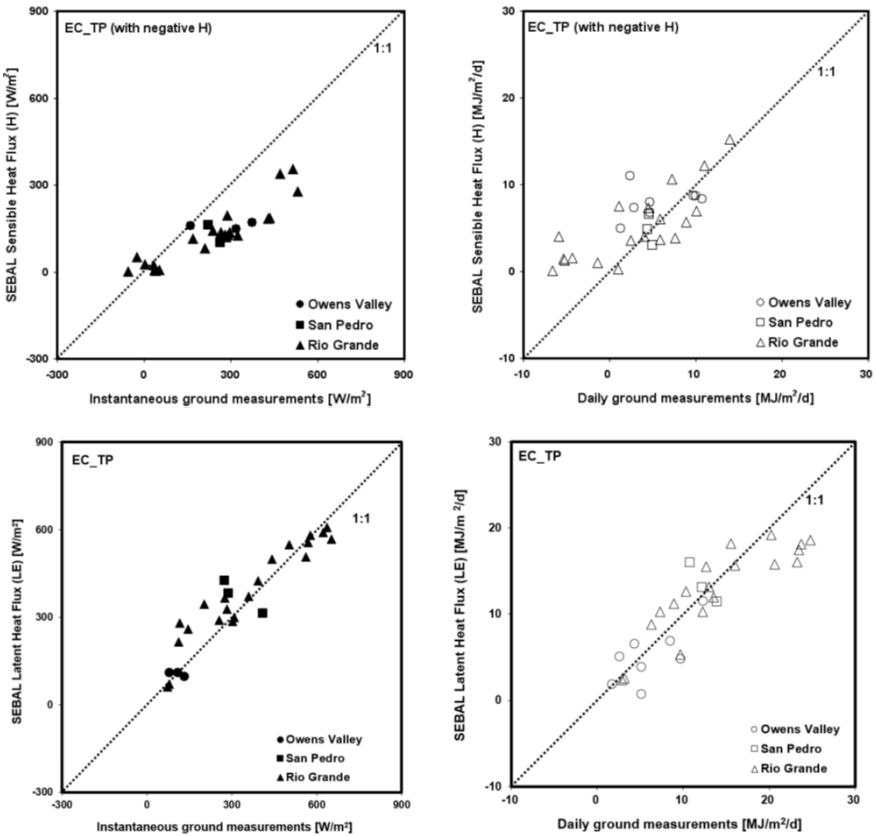

Figure 7. Comparison of sensible (*H*) and latent heat (LE) fluxes between adjusted eddy covariance tower measurements and SEBAL estimates from scenario S2 (EC_TP).

HESSD
11, 13479–13539, 2014

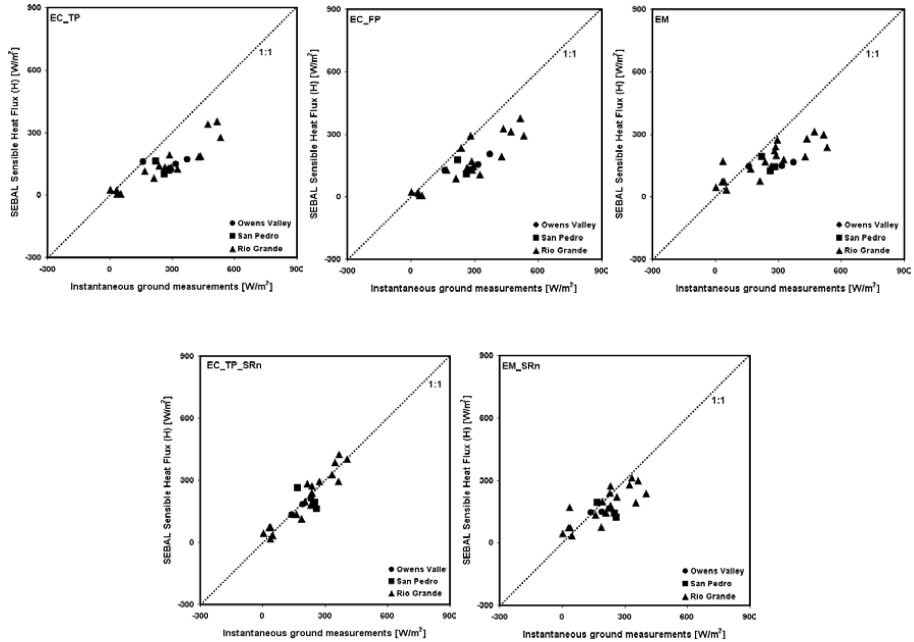

Figure 8. Comparison of instantaneous sensible heat flux (*H*) between adjusted eddy covariance tower measurements and SEBAL estimates for scenarios S1–S5.

HESSD
11, 13479–13539, 2014

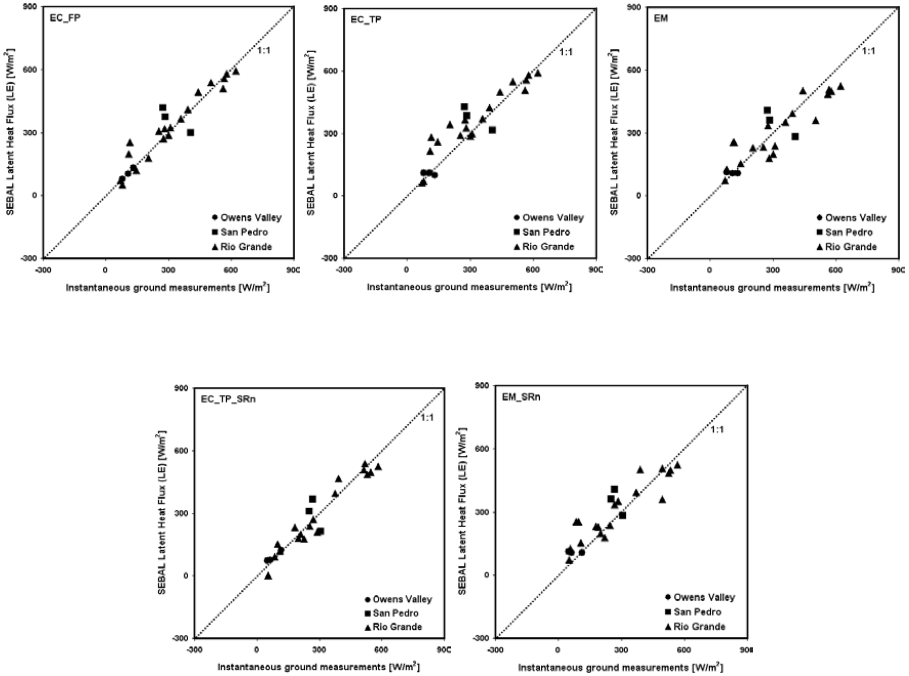

Figure 9. Comparison of instantaneous latent heat flux (LE) between adjusted eddy covariance tower measurements and SEBAL estimates for scenarios S1–S5.

HESSD
11, 13479–13539, 2014

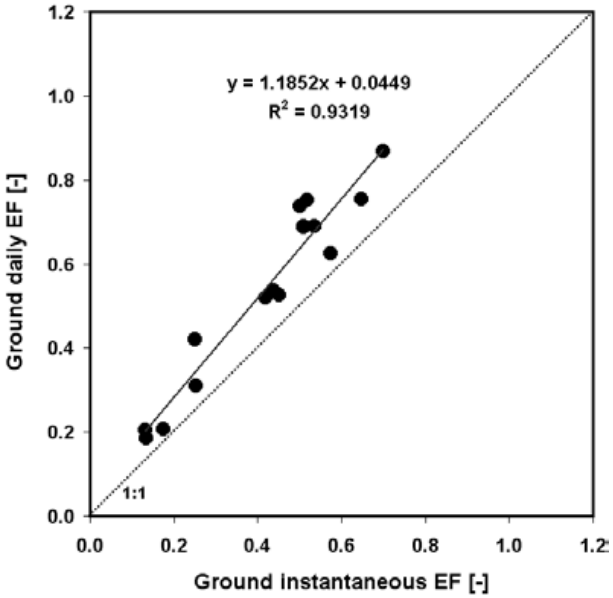

Figure 10. Comparison of satellite overpass instantaneous evaporative fraction (EF) with daytime average measured on the ground.

HESSD
11, 13479–13539, 2014

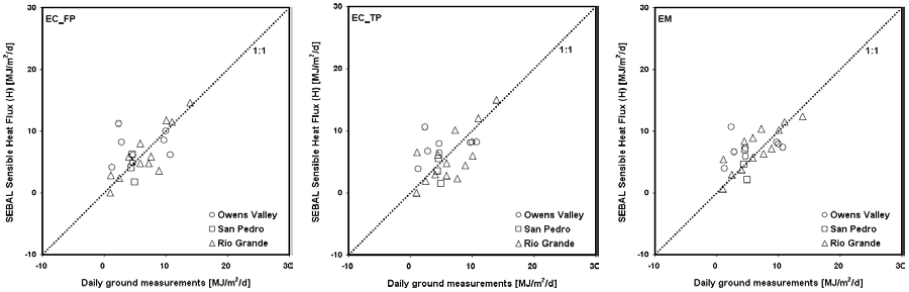

Figure 11. Comparison of daily sensible heat flux (H) between adjusted eddy covariance tower measurements and SEBAL estimates ($EF_{24} = 1.1 \times EF_{inst}$).

HESSD
11, 13479–13539, 2014

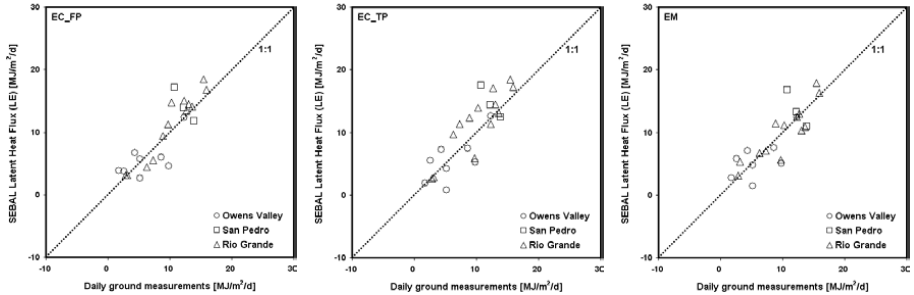

Figure 12. Comparison of daily latent heat flux (LE) between adjusted eddy covariance tower measurements and SEBAL estimates ($EF_{24} = 1.1 \times EF_{inst}$).

HESSD
11, 13479–13539, 2014

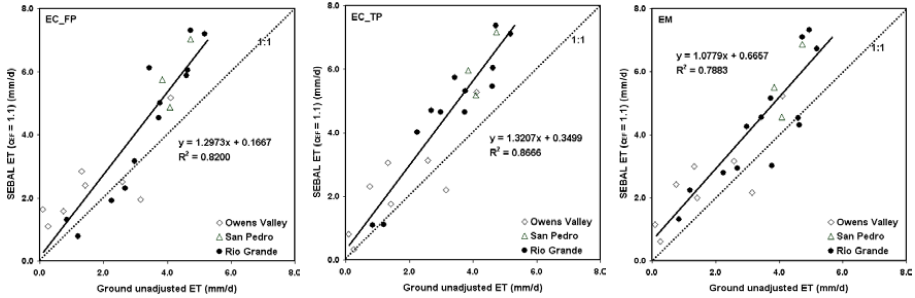

Figure 13. Comparison of ET rates determined from SEBAL with c_{EF} of 1.1 to eddy covariance ground measurements in riparian areas of the Rio Grande Valley (NM), San Pedro Valley (AZ), and Owens Valley (CA).

HESSD
11, 13479–13539, 2014